Науки о Земле
Earth sciences

UDC 550.3+550.839+550.8.056+550.8.053 http://doi.org/10.21440/2307-2091-2024-1-7-32

Integration of gravity and well data for depth-density imagining of the 3D basement complex deep structure inverse model, along with tectonic insights for further hydrocarbon exploration at El Zeit basinal area, southwest Gulf of Suez, Egypt

Ahmed Gamal Mohamed HASSAN[1,2*]
Karam Samir Ibrahim FARAG[3]
Alaa Ahmed Fahmi AREF[2]
Alexey Lazarevich PISKAREV[1]

[1] Saint Petersburg State University, Saint Petersburg, Russia
[2] Nuclear Materials Authority (NMA), Cairo, Egypt
[3] Ain shams University, Cairo, Egypt

Abstract

Relevance and purpose of the work. Salt diapirs within sedimentary strata have posed challenges in seismic interpretation within the study region, thereby impeding the construction of a comprehensive three-dimensional central basinal structure. The use of gravity data to investigate the basement fault block pattern underlying the sedimentary basin in the Gebel El-Zeit basin, located in Egypt's southwestern Gulf of Suez, is regarded as a highly recommended method for adding tectonic insights for exploring hydrocarbons in this region.

Research Methodology. The current study uses Bouguer gravity anomalies to incorporate the basement complex's lateral density model assumptions to determine the best three-dimensional basement depth for the area under consideration. The suggested methodology employs consecutive 3D spectral layered-earth inversion techniques. Various forward optimization methodologies and parameterization sequences were tested with the Oldenburg and other forward models, integrating varying constraint parameter assumptions to manage the inversion procedures.

Results and conclusions. The proposed three-stage gravity inversion scheme is intended to discover the optimal depth-density solution while minimizing computational data mismatch to the greatest extent possible. By identifying appropriate parameters for a 3D depth-density model solution, the current study applies statistical analysis to outline the relief of the basement and its complex lateral density distribution. With zero regional gravity offset and DC-shift, there was no mean error, allowing the lateral density model to be optimally constrained. Correlating depth data from multiple stratigraphic-control wells drilled in the inverted 3D basement model demonstrated the optimality of the basement relief in the studied area. The correlation analysis results demonstrate that the anticipated and measured depths best fit. This fitting means that the lateral density distribution of the basement complex is optimally assumed, resulting in a minimal computational depth error, revealing the high tectonics of the research area and high hydrocarbon entrapment potentiality.

Keywords: Egypt, Gulf of Suez, El Zeit Basin Area, Bouguer anomalies, spectral layered gravity inversion scheme, parameterizations and optimization.

Introduction

Gravitational anomalies inversely interact with sedimentary basin recovery, tectonic activity, and petroleum reserves. The source's depth, thickness, and shape make inferring the basement's undulating surface morphology from gravity data a nonlinear inverse issue. Different assumptions can lead to discrepancies in sedimentary basin basement depth. Forward Fast Fourier Transform (FFT) approximates undulating layers' gravitational or magnetic effects [1, 2].

The slab formula $g = 2\pi\gamma\Delta\rho t$ predicts sediment thickness at each gravity datum using only the gravitational constant g, density contrast $\Delta\rho$, and slab thickness t. nonlinearity was found using iterative modeling [3]. Subsequent papers increased the number of iterations, changed it to a density-depth function instead of a uniform density, and reassessed the fitting function.

Bott's iterative technique was modified by adjusting step sizes based on the model's observed-to-estimated gravity

✉ahmed.gamal_88@hotmail.com

anomalies [4]. A recent study showed that the convergence of the model can be accelerated by validating it through comparing the *L*2 norm of the residual vector with the previous iteration [3]. Drill hole gravity data, gamma-gamma density, and saturated and unsaturated sample densities supported the gravity hypothesis. Many authors have reported in their studies that the rate of density increase is highest at the surface, employing various mathematical models such as linear, quadratic, exponential, hyperbolic, and parabolic (e. g. [5–8]). The environment affects sediment density.

A recent study reported that there may be discrepancies between the density data and the density contrast function derived from density measurements taken at specific locations in a basin. This makes it difficult to build a depth-dependent density contrast [8]. Non-density contrast interpretation may benefit sedimentary basin gravity modeling.

The backward computing on the model's iteration field could yield the analytical solution for the gravity field of a two-dimensional polygonal body, three-dimensional rectangular prism, or complicated undulating layer [3]. Bott's technique avoids matrix multiplications and inversions, speeding up Fourier-domain operations compared to space-domain operations. Analytical formulations for polyhedral and prismatic bodies with linear density contrast functions and parabolic or cubic polynomial functions have been developed–algorithms model vertical density contrast fluctuation with depth. Several authors in their studies have documented that these approaches use an exponential or cubic polynomial fitting

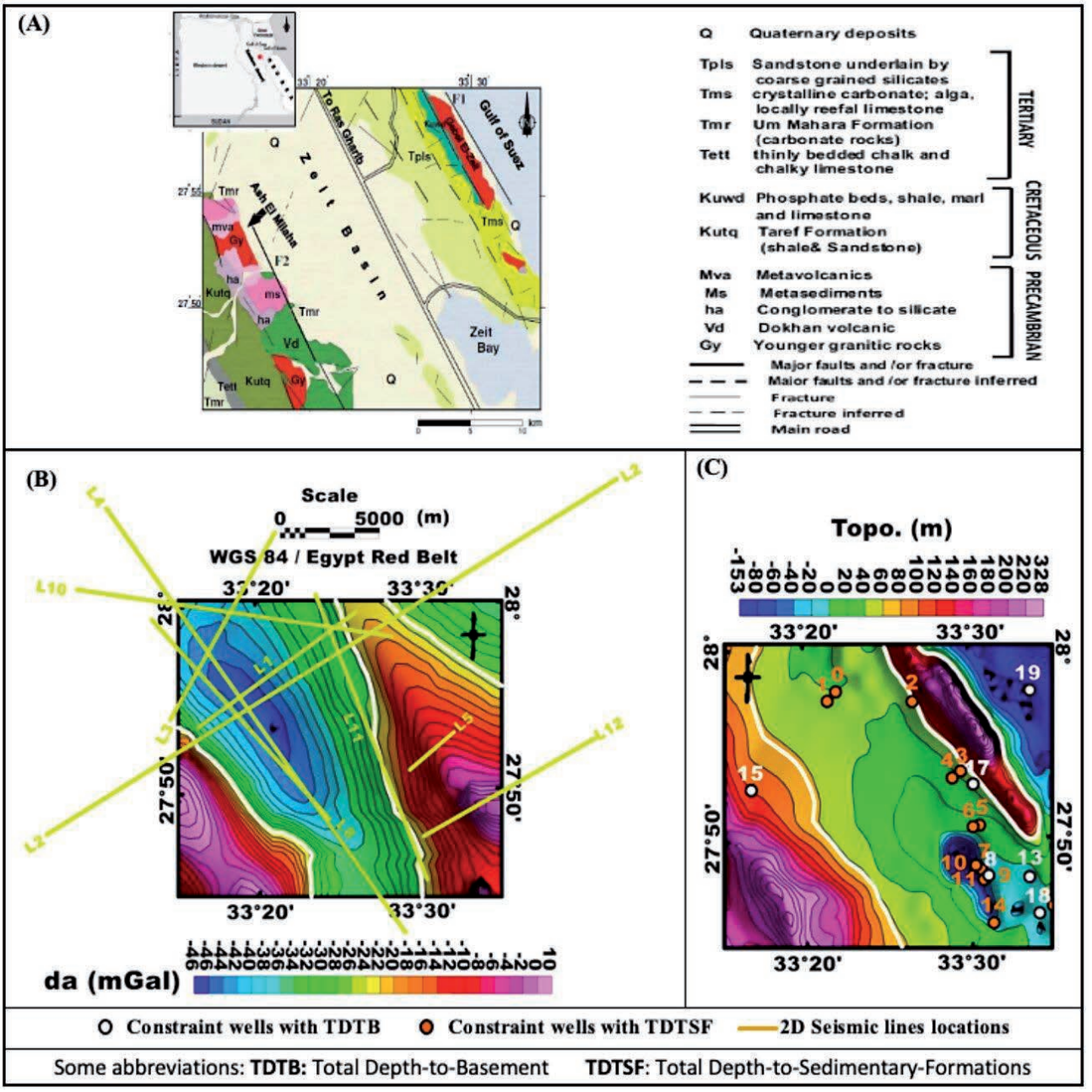

Figure 1.1. The bouguer gravity data and geological background: *A* – surface geological map [33], *B* – Bouguer anomaly contour map, *C* – Topographic map

Рисунок 1.1. Данные гравиметрии Буге и геологические предпосылки: *А* – геологическая карта поверхности [33], *Б* – контурная карта аномалии Буге, *С* – топографическая карта

Table 1. Both accessible and inaccessible total depth-to-basement constraint wells were used to set constraints on the proposed inversion scheme's inverse depth model and assess its quality [34, 35]

Таблица 1. Как доступные, так и недоступные скважины с ограничением общей глубины до фундамента, которые использовались для установки ограничений на обратную глубинную модель предлагаемой схемы инверсии и оценки ее качества [34, 35]

Well symbol	Well Name	Total Drilled Depth, m	Company	Status
1st group / wells with T.D Reached Rock Unit ***[Basement] @ geologic age/Pre-Cambrian***				
*W*8	C9A–1	2577	Conco	Abandoned tested oil and gas
*W*13	QQ89–11	1129	DEOCO	Abandoned
*W*15	Wadi Dib #1	3769	CHEV EGY	Abandoned
*W*17	Gazwarina # 1	2162	Marathon	Suspended oil
*W*18	QQ89–3	2908	SUCO	Abandoned
*W*19	ERDMA–2	4051	Published [36]	
2nd group / wells with T.D Reached Rock Unit ***[Nubia Sandstone (Nu)] @ geologic age/Carboniferous-Jurassic***				
*W*2	Kabrite west-1	1272	Petrozeit	Abandoned oil stain
*W*3	Gazwarina-2	1272	Marathon	Abandoned oil shows
*W*5	Gebel El Zeit-west-1	1966	Deminex	Abandoned
*W*6	Gebel El Zeit-west-2	2195	Deminex	Abandoned
*W*11	East Ras Gemsa-4	2542	Gupco	Abandoned gas shows
3rd group / wells with T.D Reached Rock Unit ***[Matulla Formation (Ma)] @ geologic age/Upper Cretaceous***				
*W*9	Khalig El Zeit-1	2509	Devon	Abandoned
*W*10	East Ras Gemsa-2	2538	Gupco	Abandoned
*W*16	Zeit Bay 1	4452	CHEV EGY	Abandoned
4th group / wells with T.D Reached Rock Unit ***[Nukhul Formation (Nuk)] @ geologic age/Lower Miocene***				
*W*0	Gebel El Zeit-2	3743	GPC	Abandoned
5th group / wells with T.D Reached Rock Unit ***[Rudies Formation (Ru)] @ geologic age/Lower Miocene***				
*W*1	Ramadan-1	3760	GPC	Abandoned oil and gas shows
*W*4	Gazwarina-3	951	Marathon	Abandoned
*W*7	C9A-3	2122	Conoco	Abandoned
*W*14	C9B-1	3183	Conoco	Abandoned

function (e. g. [6, 9–11, 12]). A recent study demonstrated in its review that Bott's method was employed to evaluate the gravitational impact of the increasing density of the basement and suggested solutions for reducing it [13]. Yucca Flat Basin isostatic anomalies have been examined in Nevada.

The basement geometry in the interpretation of gravity data is estimated using the Tikhonov's regularized inversion method [14]. Converting subsurface columns into prisms with known horizontal dimensions and densities allows the calculation of column thickness. The $L2$ norm of the discrete first-order derivative of the model goal function helps regularize the solution. The $L1$ norm of the discrete derivative total variation function is used to avoid penalizing quick morphological changes during basement depth inversion [15]. Nonlinear inversion smooths and blocks the model [16]. Density contrast splits the research region into smooth and blocky inversions. Lp model norm decreases after final inversion.

A composite regularizing function adjusts model smoothness in the target region to minimize an objective function [17]. Edge detection or initial approximation models identify gravitational anomalies. Using nonlinear modeling, estimation of basement morphology and constant density contrast [18]. Modeling sedimentary basins might execute without basement estimators [19, 20]. Objective function stabilizers affect fundamental characteristics, regularization parameters, and model parameter limits, making regularized inversion difficult.

Multiple basement depth measurements constrain ITRESC density depth or contrast function approximations. The ITRESC methods will be tested in the El Zeit basin in the southwest portion of Egypt's Gulf of Suez, then compared.

A prior information and geological setting. The African and Arabian tectonic plates diverged in the late Oligocene and early Miocene, forming the Gulf of Suez [21, 22]. Low-angle listric normal faulting and dyke injection caused the rift's eastward half-grabens [23]. Subsidence caused the middle to late Miocene asymmetric axial grabens to migrate eastward. Faulting and uplift found in the Esh El-Mallaha intra-rift structural block in the southern Gulf of Suez from the Pliocene to the Pleistocene/Holocene [24, 25]. Gebels El Zeit and Esh El-Mallaha have metamorphic, granitic, and Dokhan volcanic rocks on their eastern and western flanks [26].

As depicted in fig. 1.1, *A*, faults *F*1 and *F*2 run NW-SE in Quaternary alluvial wadis in the Gulf of Suez, juxtaposed with Precambrian bedrocks [27, 28]. Deep-seated tectonic faults make the Gemsa-El Zeit Bay Basin complicated. The geological composition of the area includes various formations such as the Nubian Sandstone, El Mallaha Formation, Raha Formation, Thebes Formation, Nukhul Formation, as well as the Lower/Middle Miocene Rudeis and Kareem layers. Additionally, the region features Sabkhas and salt marshes [25, 29–31]. Gravimetry can improve Earth model calculations by examining the potential field with indirect constraining of stratigraphic-control wells. Table 1 lists the wells.

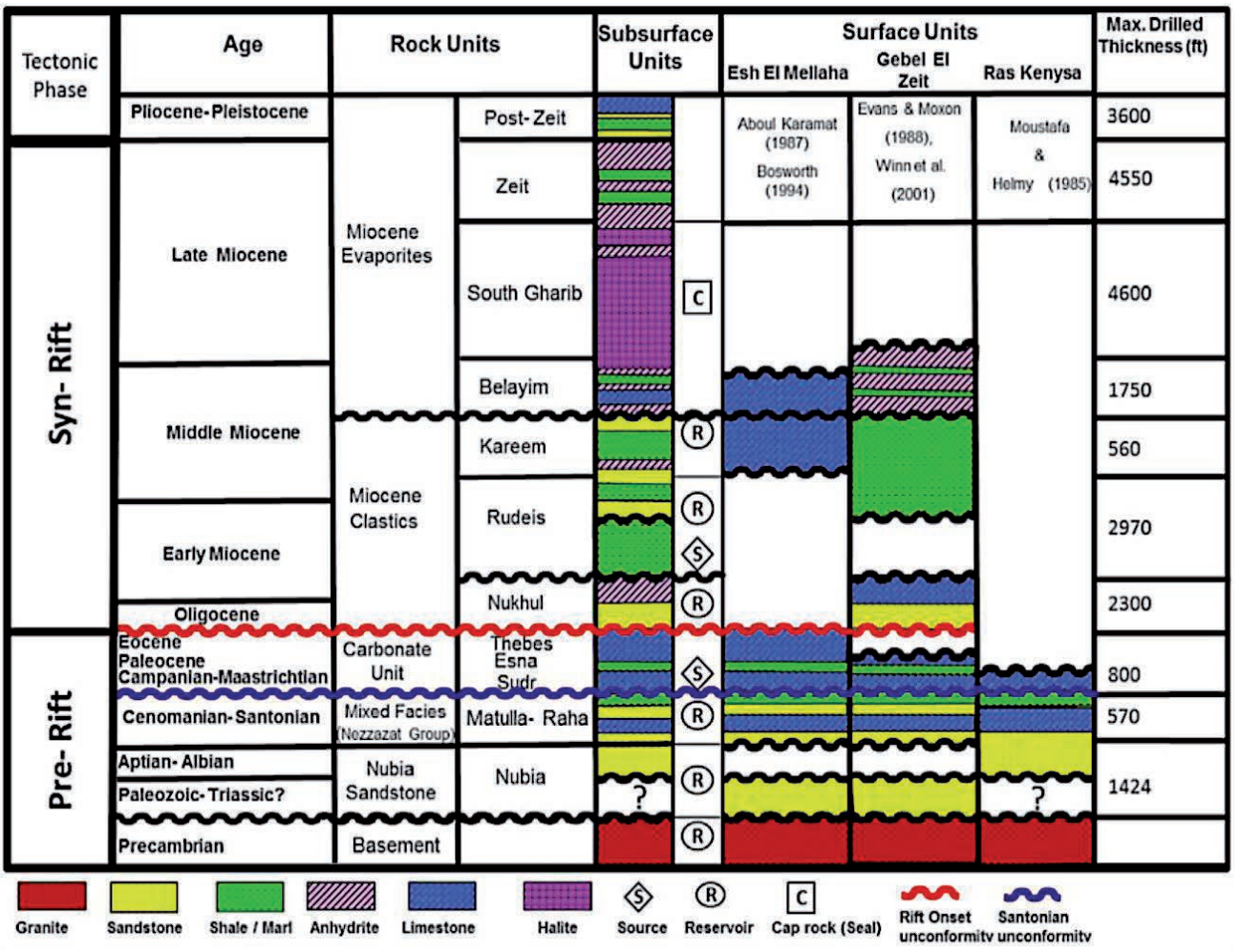

Figure 1.2. Stratigraphic geological column of southern Gulf of Suez revealing the lithology and classification of hydrocarbon potentiality at the study area of Gebel El Zeit [32]

Рисунок 1.2. Стратиграфическая геологическая колонка южной части Суэцкого залива, раскрывающая литологию и классификацию углеводородного потенциала на изучаемом участке Гебель-эль-Зейт [32]

Bouguer gravity data. The investigation used a 0.01 mGal resolution Lacoste and Worden gravimeter (Scintrex Inc., USA). The Bureau Gravimetric International (BGI) in Paris authorized the General Petroleum Corporation of Egypt (GPC) to create a gravity map of Egypt over ten years (1974–1984). A nationwide base net was created to supplement foreign company surveys. The Egyptian Academy of Scientific Research and Technology oversaw it. Re-measuring ensured precision. The raw data were exported in *x*, *y*, and *z* dimensions and gridded at 1000 m.

Figure 1, *B* shows the research region contour map colored by Bouguer anomalies. It is concluded, as seen in fig. 1.1, *A*, *B*, *C*, that Gebel El Zeit and Esh El-Mallaha have intricate basement outcrops east and west of Gemsa-El Zeit Bay, spanning a large sedimentary basin in the central region. Dual western gravity highs suggest local transmission faults at Gebel Esh El-Mallaha. Fig. 1.2 reveals the stratigraphic geological column of the southern Gulf of Suez, showing the lithology and classification of hydrocarbon potentiality at the Gebel El Zeit study area [32].

Inversion methodology

General Outline. Douglas Oldenburg's approach and others were used within the proposed three-stage inversion scheme to quantify El-Zeit basin geologic attributes in the study area. Geosoft Inc. in Toronto, ON, Canada's Oasis Montaj program's GM-SYS 3D extension sub-routine uses a popular spectral layered-earth inversion method for data reduction and filtering to help in the optimization. This method appropriately helps determine the study area's sedimentary-basement layer average density, density contrast, basement depths, and sedimentary section thickness. Oldenburg's inversion results were compared to other approaches to determine Oldenburg's constraint parameters' possibility of providing the most precisely resolved inverse model.

The proposed inversion scheme derives optimal initial and inverse models using a simple forward model and six optimization strategies with three forward and three inverse modeling scenarios in an attempt to save time and effort. Fig. 2.1, with its legend in fig. 2.2, depicts the parameterization flowchart for the proposed scheme's forward and inverse modeling processes with their three stages. (Tables 2.1; 2.2) describe all parameterization abbreviations used in our study.

Stages of the Scheme. In the initial stage, three optimization strategies were proposed: one for forward depth modeling with an unconstrained initial forward constant

Table 2. Abbreviations and classification of the parameters used to parameterize the forward and inverse models in our inversion scheme

Таблица 2. Сокращения и классификация параметров, используемых для параметризации прямой и обратной моделей в нашей схеме инверсии

Used for …	Parameter	Definition
Parameterization of root-mean-square and coefficient of variance	$(RMSD)_{ZoA \text{ or } oB1 \text{ or } oB2}$	The initial-guessed depth-to-basement root-mean-square deviation
	$(RMSD)_{ZeA \text{ or } eB1 \text{ or } eB2}$	The inverse-estimated-recovered depth-to-basement root-mean-square deviation Coefficient of variation of the initial-hypothesized depth-to-basement's root-mean-square deviation
	$(CV-RMSD)_{ZoA \text{ or } oB1 \text{ or } oB2}$	Coefficient of variation of the inverse-estimated-recovered depth-to-basement's root-mean-square deviation
	$(CV-RMSD)_{ZeA \text{ or } eB1 \text{ or } eB2}$	Coefficient of variation of the initial-hypothesized homogenous basement complex's density's root-mean-square deviation
	$(CV-RMSD)_{\rho boA \text{ or } oB1 \text{ or } oB2}$	Coefficient of variation of the inverse-estimated-recovered homogenous basement complex's density's root-mean-square deviation
	$(CV-RMSD)_{\rho beA \text{ or } eB1 \text{ or } eB2}$	Coefficient of variation of the initial-hypothesized basement complex's lateral density distribution's root-mean-square deviation
	$(CV-RMSD)_{LDDboA \text{ or } oB1 \text{ or } oB2}$	Coefficient of variation of the inversely-estimated recovered basement complex's lateral density distribution's root-mean-square deviation
	$(CV-RMSD)_{LDDbeA \text{ or } eB1 \text{ or } eB2}$	
Parameterization of depth and density model	$(DTB)a$	Actual-measured depth-to-basement
	$(DTB)_{oA \text{ or } oB1 \text{ or } oB2}$	Initial-hypothesized depth-to-basement
	$(DTB)_{eA \text{ or } eB1 \text{ or } eB2}$	Inverse-estimated depth-to-basement
	$(pB)_{oA \text{ or } oB1 \text{ or } oB2}$	Initial-hypothesized basement complex's homogenous density
	$(pB)_{eA \text{ or } eB1 \text{ or } eB2}$	Inverse-estimated-recovered basement complex's homogenous density
	$(LDDb)_{oA \text{ or } oB1 \text{ or } oB2}$	Initial-hypothesized basement complex's lateral density distribution
	$(LDDb)_{eA \text{ or } eB1 \text{ or } eB2}$	Inverse-estimated-recovered basement complex's lateral density distribution
Parameterization of density contrast model	$\Delta\rho\ (\rho b-\rho s)_{oA \text{ or } oB1 \text{ or } oB2}$	Initial-hypothesized sedimentary-basement's homogenous density contrast interface
	$\Delta\rho\ (\rho b-\rho s)_{oA \text{ or } oB1 \text{ or } oB2}$	Inverse-estimated-recovered sedimentary-basement's homogenous density contrast interface
	$\Delta\rho\ (LDDb-\rho s)_{oA \text{ or } oB1 \text{ or } oB2}$	Initial-hypothesized sedimentary-basement's lateral density contrast interface distribution
	$\Delta\rho\ (LDDb-\rho s)_{eA \text{ or } eB1 \text{ or } eB2}$	Inversely-estimated-recovered sedimentary-basement's lateral density contrast interface distribution
Parameterization of Inversion process constraint parameters	$(DC\ shift)_{eA \text{ or } eB1 \text{ or } eB2}$	DC shift
	$(Reg.offset)_{oA \text{ or } oB1 \text{ or } oB2}$	Regional offset
	$(Cnv.limit)_{eA \text{ or } eB1 \text{ or } eB2}$	Convergence limit
	$(Flt.LHC\ Limit)_{eA \text{ or } eB1 \text{ or } eB2}$	Lower high cut limit Filter
	$(Flt.UHC\ Limit)_{eA \text{ or } eB1 \text{ or } eB2}$	Upper high cut limit Filter
Parameterization of data and data misfit	$(d)_a$	Actual-observed Bouguer gravity data
	$(d)_{oA \text{ or } oB1 \text{ or } oB2}$	Initial-hypothesized Bouguer gravity data
	$(d)_{eA \text{ or } eB1 \text{ or } eB2}$	Inverse-estimated Bouguer gravity data
	$(\Delta d)_{eA \text{ or } eB1 \text{ or } eB2}$	Residual bouguer gravity as an indicator for inverse-estimated-recovered data misfit

Note: The abbreviations *A*, *B*1, and *B*2 are used to represent the three stages of parameterization. These parameters mentioned in tables 2.1 and 2.2 are initialized and estimated once for model *A* (representing the first stage of parameterization), again for model *B*1 (representing the second stage of parameterization), and finally for model *B*2 (representing the third stage of parameterization).

mean depth surface, another for forward density modeling with initial forward density constraint assumptions of a 3D homogeneous two-layered density model, and a third for depth inverse modeling that combines both strategies to recover Oldenburg's model with minimal error.

In the second stage, three other optimization strategies were proposed. The paper suggests three depth and density modeling strategies: forward depth modeling, forward density modeling, and density inverse modeling. The first strategy entails utilizing an initial depth surface to make depth predictions with variable errors, gradually decreasing errors with each guess. The second strategy limits density contrast guesses by laterally splitting density contrast estimates into homogenous-heterogenous two-layered density models. The third strategy combines the second stage's two above-mentioned forward strategies to find the best inverse-density solutions possible.

The third final stage employed three additional optimization strategies: one for forward depth modeling, which employs an unconstrained version of the forward variable depth constraint assumptions derived from trials of inverted 3D possible depth models with varying depth calculation errors; another for forward density modeling, which employs the constrained version of the second stage's inverted lateral density possible

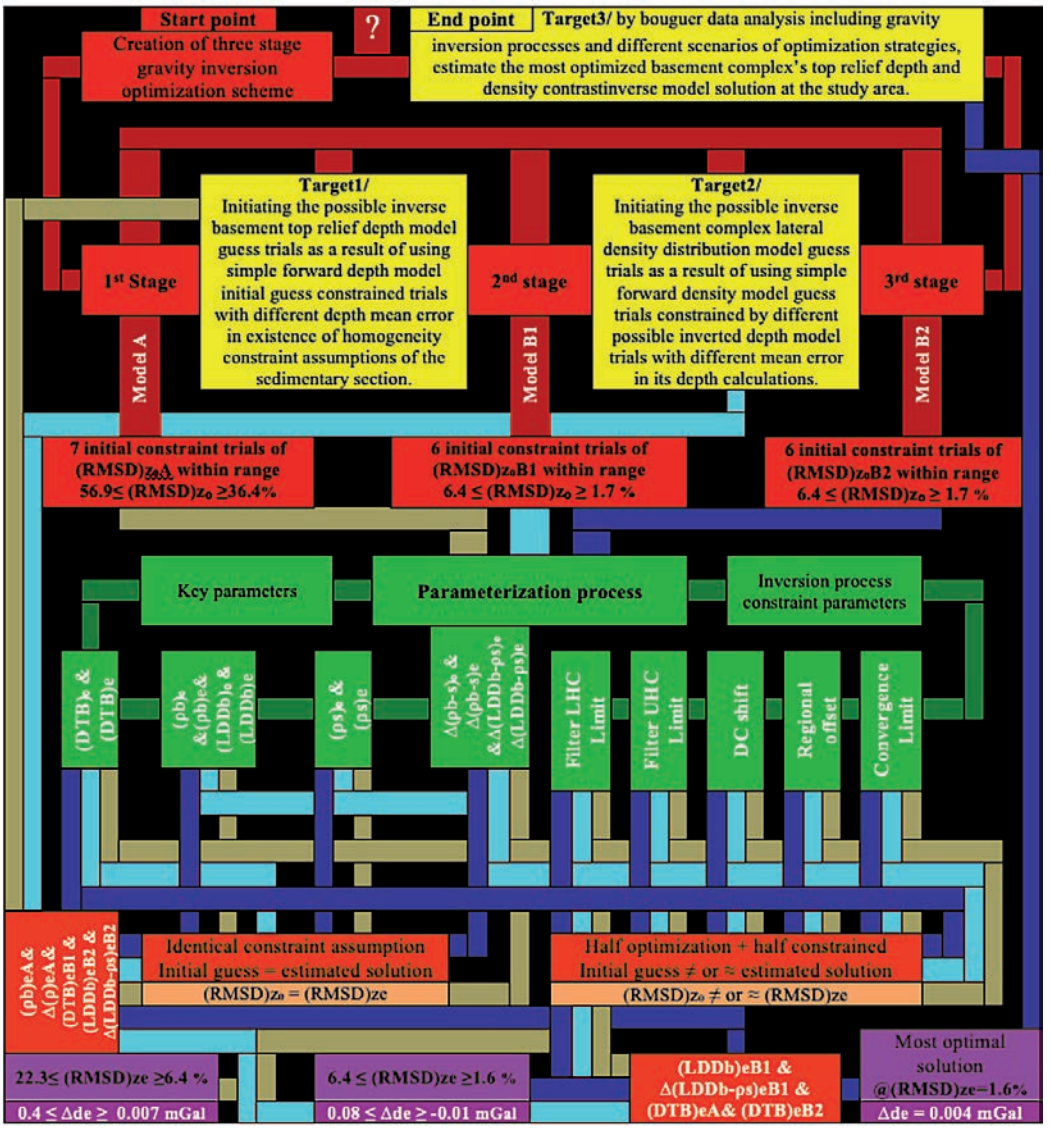

Figure 2.1. The flowchart for the three-stage inversion scheme utilized in this study includes optimization scenarios performed at each stage and between stages. Table 2 has a comprehensive list of abbreviations. Fig. 2.2 depicts a legend for this flowchart colorization

Рисунок 2.1. Блок-схема трехэтапной схемы инверсии, используемой в этом исследовании, включает сценарии оптимизации, выполняемые на каждом этапе и между этапами. В табл. 2 приведен полный список сокращений. На рис. 2.2 изображена легенда для цветовых обозначений данной блок-схемы

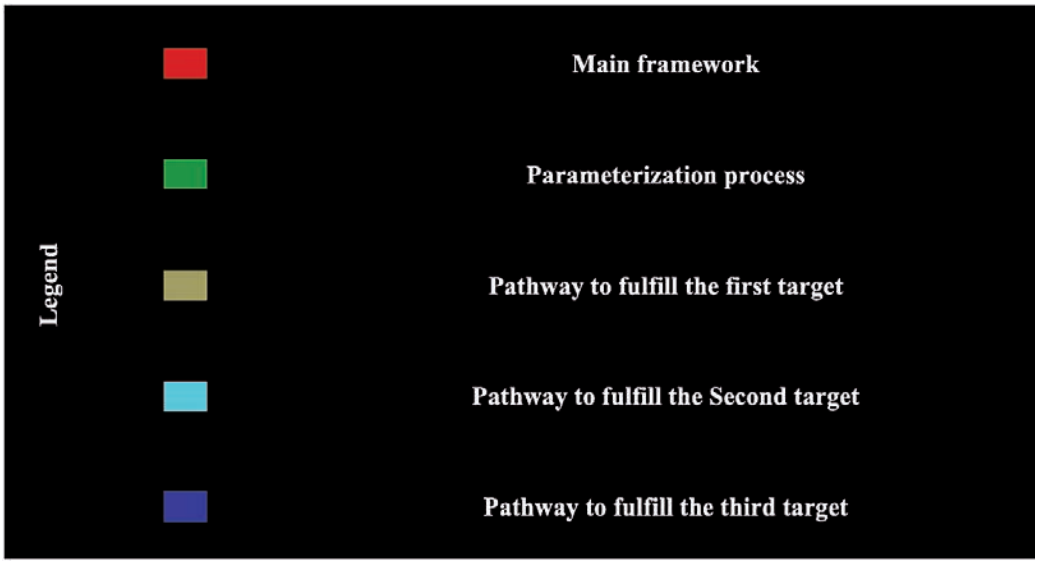

Figure 2.2. The legend for the proposed inversion scheme flow chart shown in fig. 2.1

Рисунок 2.2. Легенда к предлагаемой блок-схеме инверсии, представленной на рис. 2.1

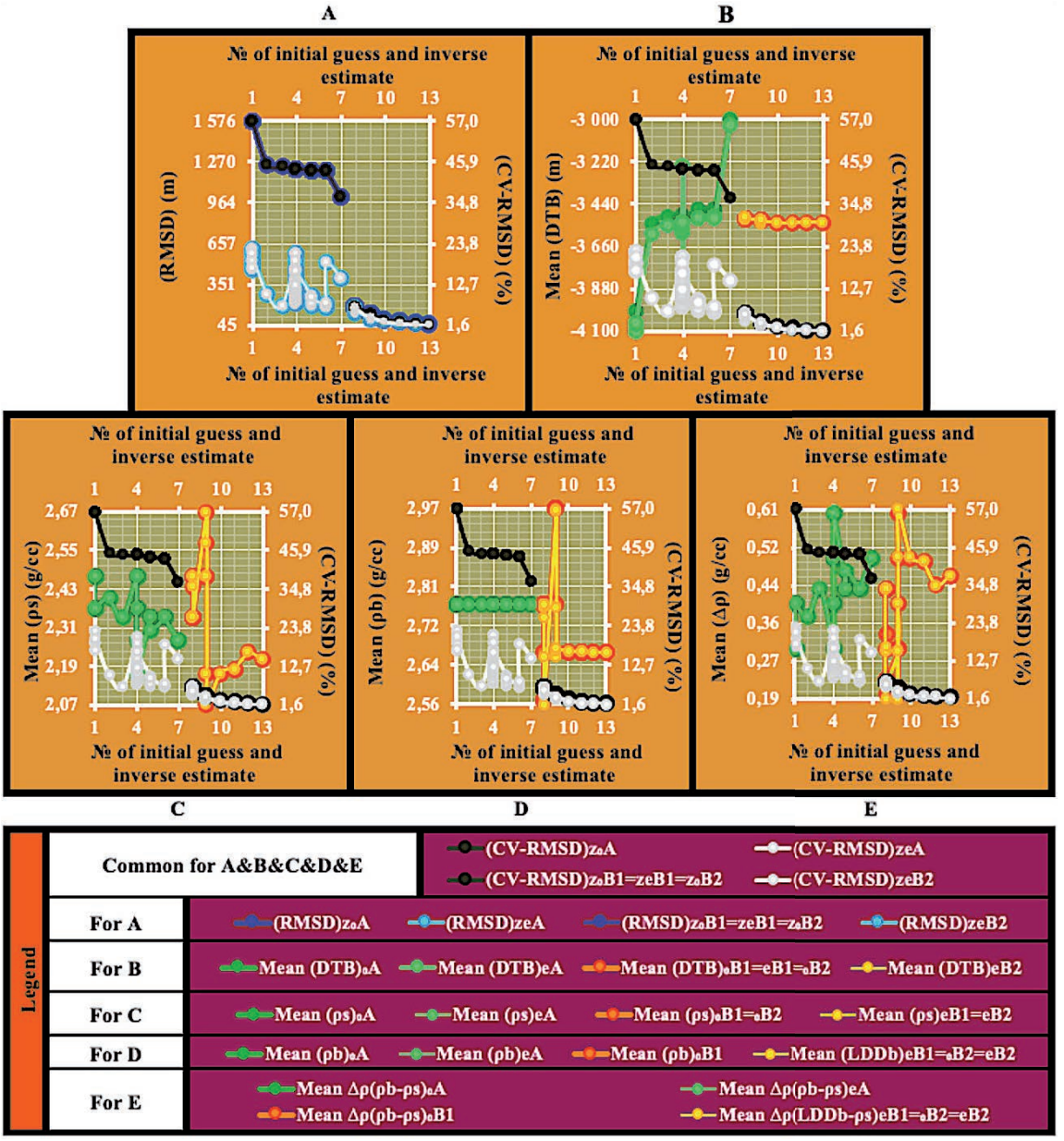

Figure 3.1. The three-stage optimization procedure for forward and inverse parameters guesses and recovers basement depth-density and basement-sedimentary interface density contrast models from five graphs with a root-mean-square coefficient of variance of 1.62% at the thirteenth trial. The abbreviations in tables 2.1 and 2.2

Рисунок 3.1. Трехэтапная процедура оптимизации для прямых и обратных параметров, которая угадывает и восстанавливает модели плотности глубины фундамента и контрастной плотности границы раздела фундамент–осадочные породы из пяти графиков со среднеквадратичным коэффициентом дисперсии 1,62 % в тринадцатой пробе. Сокращения в табл. 2.1 и 2.2

models; and a third for inverse depth modeling. During the second and third rounds of the suggested inversion process, the low error was achieved through iterative refinement of depth-density model solutions within the density contrast constrained-unconstrained optimization framework.

Results and discussion

A Comparison of the best-possible models in three stages. Three minimal-error inverse models were constructed from the three best forward models, representing the optimal result of the proposed three-stage inversion scheme. (Figs 3.1, 3.2, 3.3, 3.4) demonstrate how mean depth error guessing trials limited these. Each stage creates forward models and inverse solutions using distinct strategies. The assessment of inversion findings in the research region and individual sites showed the model's capacity to reduce computation inaccuracies and ensure dependability.

Optimal parameterization sequences, including first-stage parameters, started with 43.6% inaccuracy, the forward models with initial values Z_0 –3470 m, ρb_0 2.77 g/cc, ρs_0 2.34 g/cc, $\Delta\rho(\rho b-\rho s)_0$ 0.43 g/cc, Δd_0 37.65 mGal, *DC* shift 37.652 mGal, filter LHC limit 14000 m, filter UHC limit 7500 m, convergence limit 0.01 mGal, and regional offset 0 mGal. These inputs started forward modeling with 43.6% inaccuracy. The second stage included these forward parameters: Z_0 –3536 m, ρb_0 2.67 g/cc, ρs_0 2.21 g/cc, $\Delta\rho(\rho b - \rho s)_0$ 0.46 g/cc, Δd_0 42.661 mGal, *DC* shift 42.661 mGal, filter LHC limit 10000 m, filter UHC limit 9600 m, convergence limit 0.0054 mGal, and regional offset 0 mGal. Forward modeling guessing,

in this case, decreased to 1.78% inaccurate. The third stage finally initiated with these initial parameters: Z_0 –3536 m, $LDDb_0$ 2.6706 g/cc, ρs_0 2.21 g/cc, $\Delta\rho(LDDb-\rho s)_0$ 0.4606 g/cc, Δd_0 42.670 mGal, *DC* shift 42.670 mGal, filter LHC limit 20000 m, filter UHC limit 15 000 m, convergence limit 0.0001 mGal, and regional offset 0 mGal, constrained with the 1.78% forward modeling guessing inaccurate.

The parameters estimated with 6.4 % inaccuracy recovered the optimal first-stage inverse model with these parameters: Ze –3513 m, ρbe 2.77 g/cc, ρse 2.34 g/cc, $\Delta\rho(\rho b-\rho s)e$ 0.43 g/cc, Δde 0.0506 mGal, *DC* shift 37.652 mGal, filter LHC limit 14000 m, filter UHC limit 7500 m, convergence limit 0.01 mGal, and regional offset 0 mGal. The optimal 1.78%

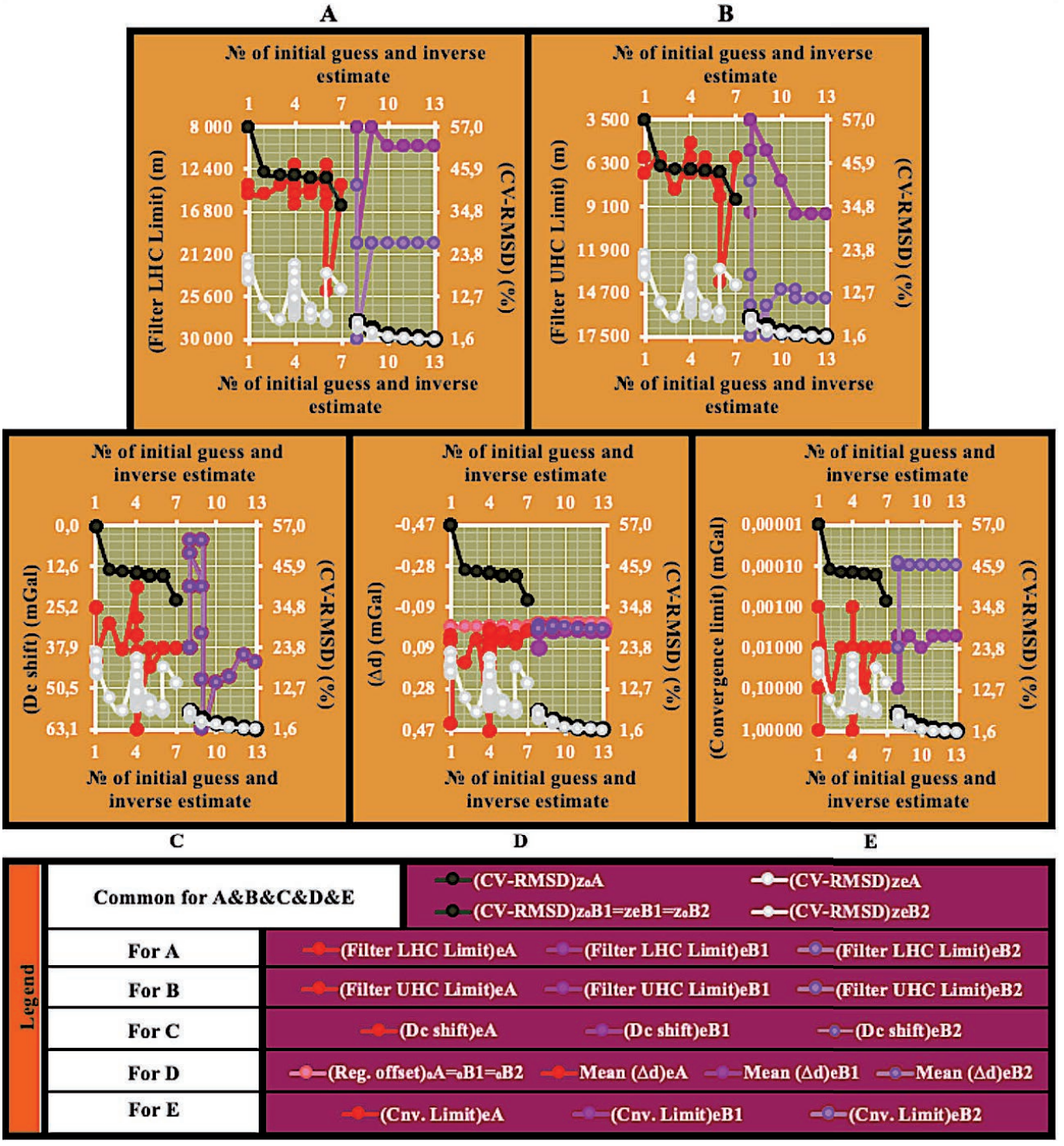

Figure 3.2. The parameterization expressed across five graphs shows that the proposed inversion scheme used a three-stage optimization process for six inversion process inner constraint parameters to provide the optimal solution with a root-mean-square coefficient of variance of only 1.62% after thirteen trials. Both tables 2.1 and 2.2 list abbreviations extensively

Рисунок 3.2. Параметризация, выраженная на пяти графиках, показывает, что в предложенной схеме инверсии использовался трехэтапный процесс оптимизации для шести параметров внутренних ограничений процесса инверсии, чтобы обеспечить оптимальное решение со среднеквадратичным коэффициентом дисперсии всего 1,62 % после тринадцати проб. В табл. 2.1 и 2.2 подробно перечислены сокращения

inaccurate-constrained inverse model for the second stage was constrained using the following parameters: (*Ze* –3536 m, *LDDbe* 2.6706 g/cc, ρ*se* 2.21 g/cc, Δρ(*LDDb*–ρ*s*)*e* 0.4606 g/cc, Δ*de* 0.0094 mGal, *DC* shift 42.661 mGal, filter LHC limit 10000 m, filter UHC limit 9600 m, convergence limit 0.0054 mGal, and regional offset 0 mGal). The optimal inverse model for the third stage was finally estimated with 1.63% inaccuracy after recovering the following parameters: (*Ze* –3534.6 m, *LDDbe* 2.6706 g/cc, ρ*se* 2.21 g/cc, Δρ(*LDDb*–ρ*s*)*e* 0.4606 g/cc, Δ*de* 0.0045 mGal, *DC* shift 42.670 mGal, filter LHC limit 20 000 m, filter UHC limit 15000 m, convergence limit 0.0001 mGal, and regional offset 0 mGal).

Connecting the three-stage best-possible inverse parameterization estimates and their inaccuracies assessed

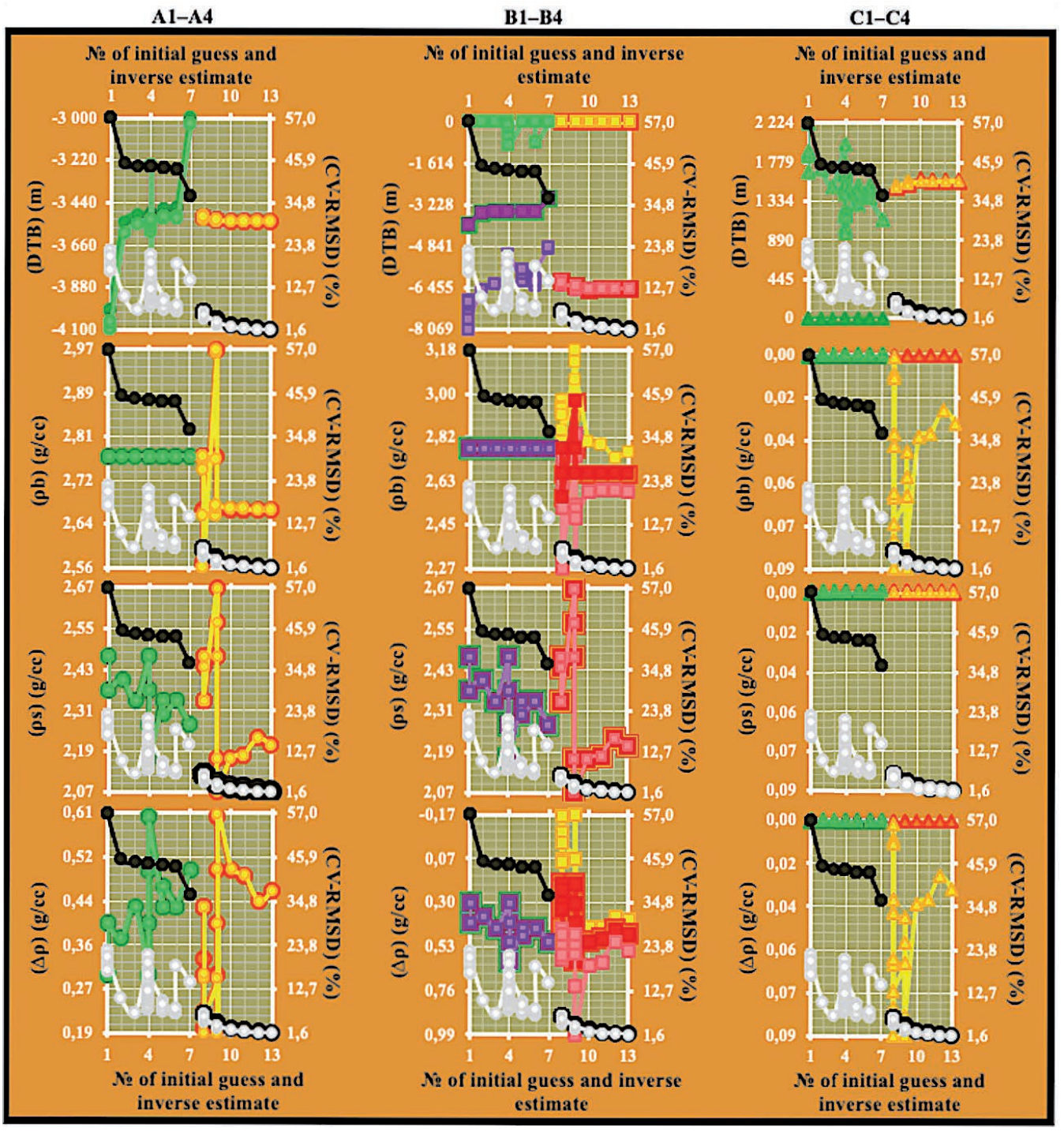

Figure 3.3. Three-stage optimization constrained by thirteen trials of decreasing root-mean-square coefficient of variance of initial guesses to recover interfaced basement-sedimentary depth-density and density contrast model solutions for mean (*A*1–*A*4), maximum (*B*1–*B*4), and standard deviation (*C*1–*C*4) parameters. Fig. 3.4 shows the legend – tables 2.1 and 2.2 list abbreviations

Рисунок 3.3. Трехэтапная оптимизация, ограниченная тринадцатью пробами уменьшения среднеквадратического коэффициента дисперсии первоначальных предположений для восстановления решений модели сопряженных глубин фундамента и осадочных пород и контраста плотности для средних (A1–A4), максимальных (B1–B4) и стандартных (C1–C4) параметров отклонения. На рис. 3.4 представлена легенда – в табл. 2.1 и 2.2 приведены сокращения

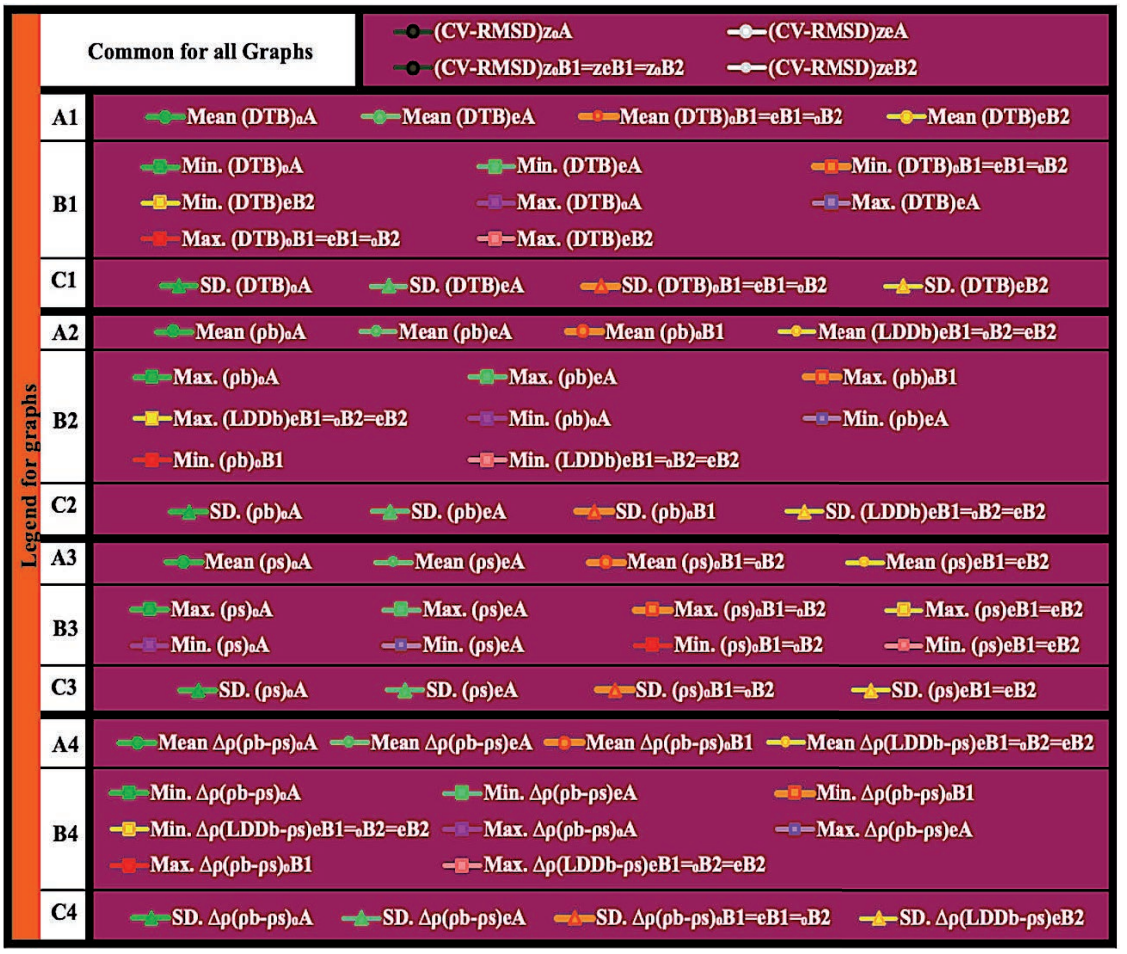

Figure 3.4. Legend of the data analysis, which is graphically represented in fig. 3.3
Рисунок 3.4. Легенда анализа данных, которая графически представлена на рис. 3.3

our scheme's optimality within this sequence: 6.4% for the first stage, 1.78% for the second, and 1.63% for the third. Iterative optimization with a zero regional offset data-misfit constraint in three stages caused this inaccuracy sequence. This optimality was obtained after these three-stage optimization sequences: mean depth (–3513, –3536, –3534.6 m), mean density contrast (0.43, 0.4606, 0.4606 g/cc), filter LHC limit (14 000, 10 000, 20 000 m), filter UHC limit (7500, 9600, 15 000 m), convergence limit (0.01, 0.0054, 0.0001 mGal), and *DC* shift (37.652, 42.661, 42.670 mGal).

The parameters estimated with 6.4 % inaccuracy recovered the optimal first-stage inverse model with these parameters: *Ze* –3513 m, ρbe 2.77 g/cc, ρ*se* 2.34 g/cc, Δρ(ρ*b*–ρ*s*)*e* 0.43 g/cc, Δ*de* 0.0506 mGal, *DC* shift 37.652 mGal, filter LHC limit 14000 m, filter UHC limit 7500 m, convergence limit 0.01 mGal, and regional offset 0 mGal. The optimal 1.78% inaccurate-constrained inverse model for the second stage was constrained using the following parameters: (*Ze* –3536 m, *LDDbe* 2.6706 g/cc, ρ*se* 2.21 g/cc, Δρ(*LDDb* – ρ*s*)*e* 0.4606 g/cc, Δde 0.0094 mGal, *DC* shift 42.661 mGal, filter LHC limit 10000 m, filter UHC limit 9600 m, convergence limit 0.0054 mGal, and regional offset 0 mGal). The optimal inverse model for the third stage was finally estimated with 1.63% inaccuracy after тrecovering the following parameters: (*Ze* –3534.6 m, *LDDbe* 2.6706 g/cc, ρse 2.21 g/cc, Δρ(*LDDb* – ρ*s*)*e* 0.4606 g/cc, Δ*de* 0.0045 mGal, *DC* shift 42.670 mGal, filter LHC limit 20 000 m, filter UHC limit 15000 m, convergence limit 0.0001 mGal, and regional offset 0 mGal).

Connecting the three-stage best-possible inverse parameterization estimates and their inaccuracies assessed our scheme's optimality within this sequence: 6.4% for the first stage, 1.78% for the second, and 1.63% for the third. Iterative optimization with a zero regional offset data-misfit constraint in three stages caused this inaccuracy sequence. This optimality was obtained after these three-stage optimization sequences: mean depth (–3513, –3536, –3534.6 m), mean density contrast (0.43, 0.4606, 0.4606 g/cc), filter LHC limit (14 000, 10 000, 20 000 m), filter UHC limit (7500, 9600, 15 000 m), convergence limit (0.01, 0.0054, 0.0001 mGal), and *DC* shift (37.652, 42.661, 42.670 mGal).

Quantitative interpretation. We evaluated with geologic correlation the key and constraint model parameters that led to the optimal thirteenth trials in the initial forward guesses and inverse estimations (Figs 4–6) of depth, density, and density contrast. These trials recover the basement complex depth-density model's whole 3D optimal image from our third-last-stage inversion scheme's best-possible parameterization sequence. The following interpretations quantitatively represent this evaluation:

The thirteenth-estimate, which represents model *B*2 in (Fig. 4), shows the third stage's optimal depth inversion procedure. The initial forward depth model has a 1.78% depth inaccuracy due to guessing parameters of Mean DTB_0 –3535.9, Max DTB_0 –6460.9,

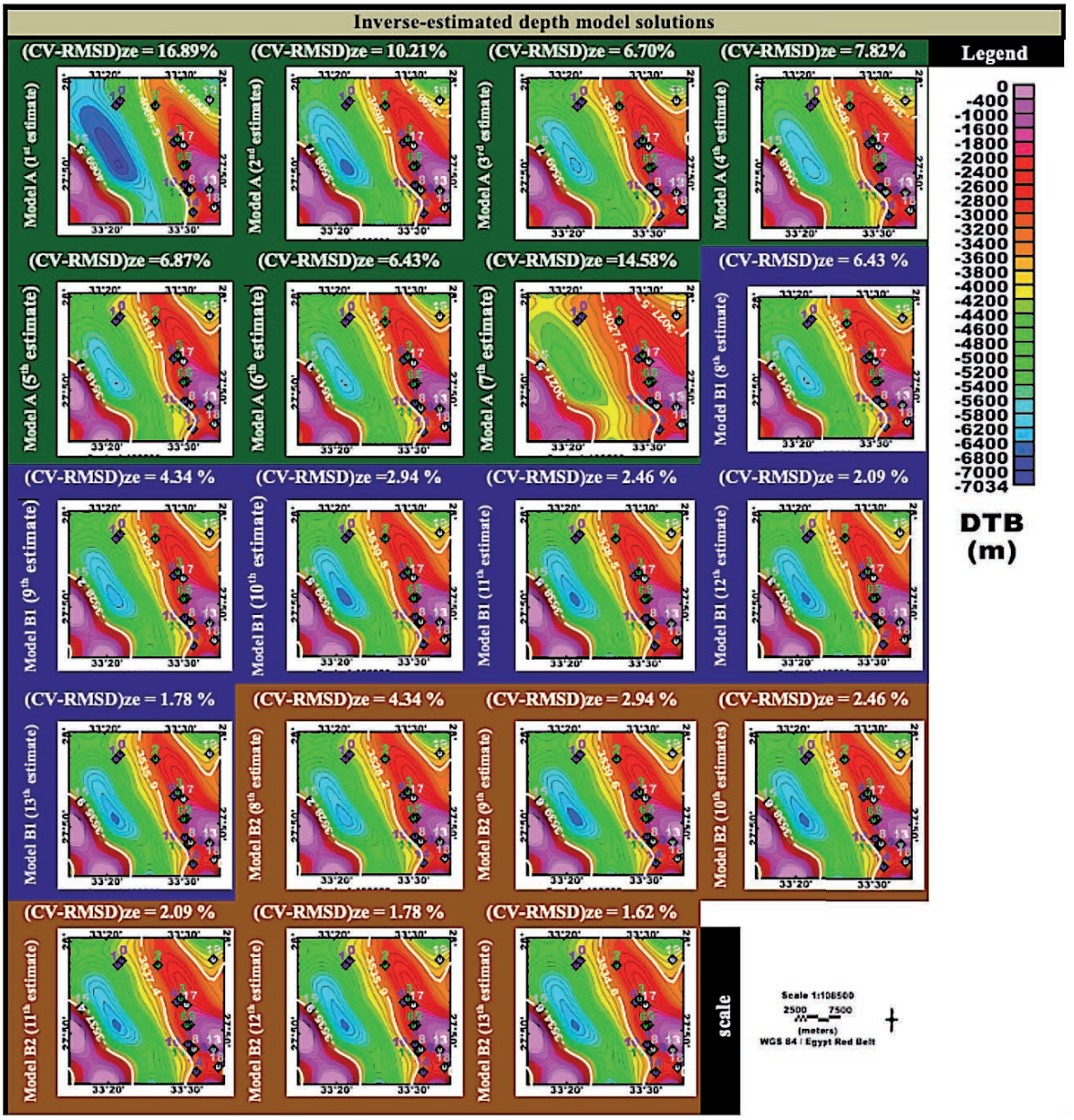

Figure 4. Three-stage depth-to-basement estimation trials are depicted by three depth models: inverse model *A* (green background, first stage), constrained model *B*1 (blue background, second stage), and inverse model *B*2 (brown background, third stage). These three-stage depth findings help to examine the optimality of three forward modeling methods with distinct scenarios

Рисунок 4. Трехэтапные испытания по оценке глубины до фундамента изображены тремя моделями глубины: обратной моделью *A* (зеленый фон, первый этап), ограниченной моделью *B*1 (синий фон, второй этап) и обратной моделью *B*2 (коричневый фон, третий этап). Эти трехэтапные измерения глубины помогают изучить оптимальность трех методов прямого моделирования с различными сценариями

Min DTB_0 0, and *SD* DTB_0 1564.8 m. Inversely estimated depth parameters (Mean *DTBe* –3534.6, Max *DTBe* –6453.2, Min *DTBe* 0, and *SD DTBe* 1567.4 m) have a 1.63% depth error. The forward beginning mean-depth parameter closely matches the optimal basement mean depth in the study area. The basement geological alteration of the thirteenth-estimate of fig. 4 suggests a Graben system underneath the research area, created by two principal normal faults running from the surface to significant depths – the geological map's basement rocks outcrop at Min *DTBe* = 0 m, the second-best fit. The third-best maximum depth parameter shows that the two principal normal faults in the center basin stretch to –6453.2 meters below sea level. Parallel to the southeast-to-northwest normal faults, secondary faults flank the central graben. Two basement complex normal faults formed the sedimentary basin between the eastern El-Zeit and western Esh El Mallaha mountain ranges. The appropriate sedimentary basin depth model can be produced by identifying the basement relief.

The third stage of the inversion scheme used optimal initial forward density guessing parameters, including Mean $LDDb_0$ 2.6706, Max $LDDb_0$ 2.7558, Min $LDDb_0$ 2.5935, and *SD* $LDDb_0$ 0.0294 g/cc, with an error constraint assumption of 1.74%. The best-constrained density parameters of Mean *LDDbe* 2.6706, Max *LDDbe* 2.7558, Min *LDDbe* 2.5935, and *SD LDDbe* 0.0294 g/cc, respectively produced a density solution with a computed depth inaccuracy of 1.63%. The mean density parameter of 2.6706 mGal in Model *B*2, represented by the thirteenth-

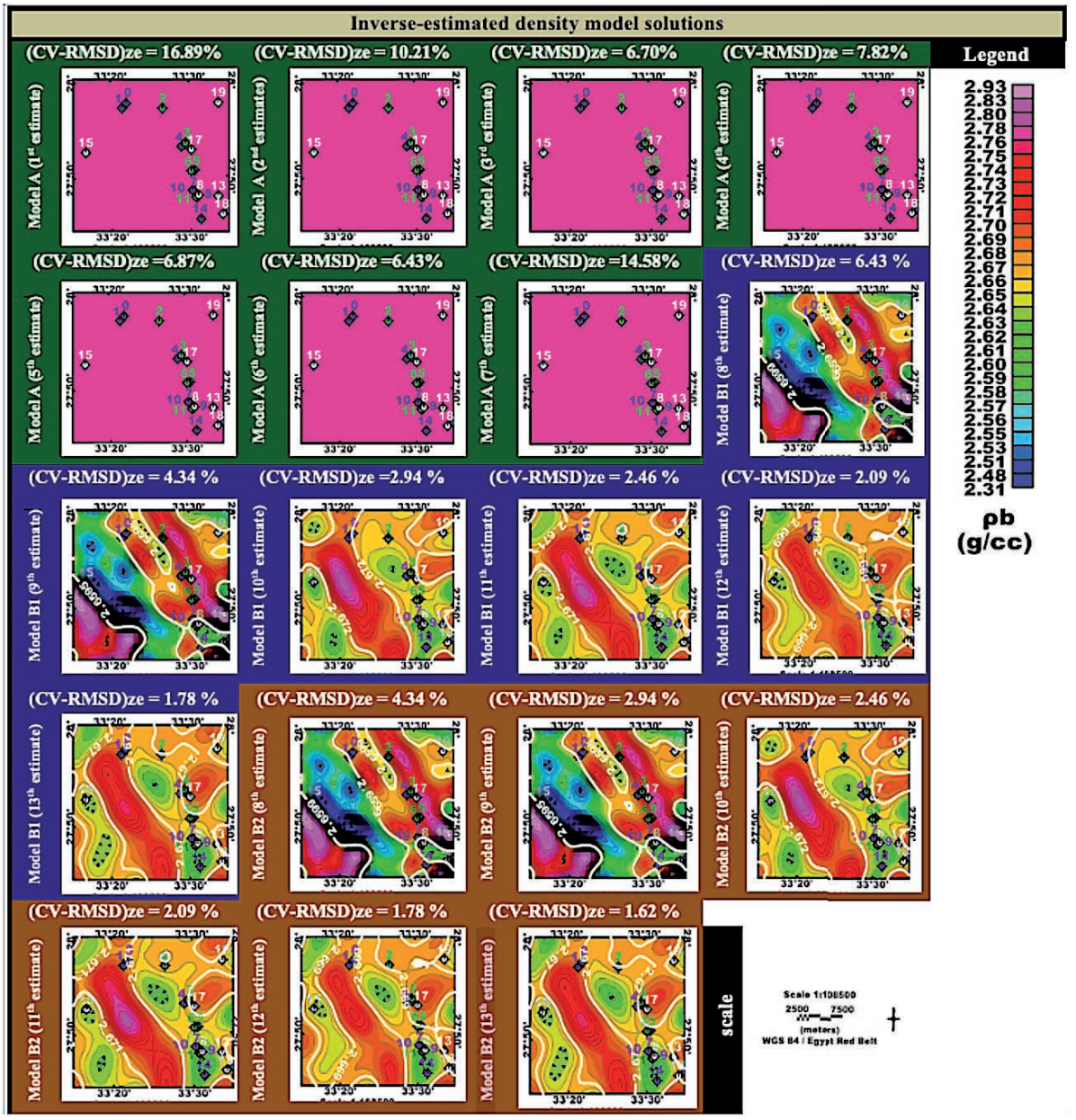

Figure 5. Three-stage basement complex lateral density estimated trials represented three models *A* (for 1st stage), *B*1 (for 2nd stage), and *B*2 (for 3rd stage). These trials reveal the constraining process used in between the second and third stages for checking the density lateral optimization procedure leading to the optimality of the basement depth with 1.62% minimal root-mean-square coefficient of variance

Рисунок 5. Трехэтапные пробы по оценке латеральной плотности комплекса фундамента представляли собой три модели *A* (для 1-го этапа), *B*1 (для 2-го этапа) и *B2* (для 3-го этапа). Эти пробы выявляют процесс ограничения, используемый между вторым и третьим этапами для проверки процедуры горизонтальной оптимизации плотности, приводящей к оптимальности глубины фундамента с минимальным среднеквадратичным коэффициентом дисперсии 1,62 %

estimate in fig. 5, suggests that granitic basement rocks dominate the basement complex's lateral mean density distribution in the research area. Acidic igneous rock densities range from 2.5935 to 2.7558 g/cc, represented by *LDDbe*'s second and third density parameters. These characteristics help determine basement depth and match pre-existing data. Inverse modeling within this density range helps recover the optimal inverse estimated depth model – the correlation between the thirteenth estimate in (Figs 4, 5) display surface basement rocks.

The optimal sixth inverse depth modeling trial's third stage used the basement-sedimentary interface as a density contrast constraint. Optimal initialized forward $\Delta\rho(LDDb-s)_0$ modeling parameters of Mean 0.4606, Max 0.5458, Min 0.3835, and *SD* 0.0294 g/cc, used to account for $\Delta\rho(LDDb-s)e$ best-possible inverse-constrained density contrast model with constrained parameters of Mean 0.4606, Max 0.5458, Min 0.3835, and SD 0.0294 g/cc. Inverse density contrast assumptions were optimized according to depth optimization. The thirteenth-estimate, which represents model *B*2 in (Fig. 6) shows the mean lateral density contrast Mean $\Delta\rho(LDDb-s)e$ 0.4606 g/cc optimally distributed on the sedimentary-basement interface in the research area. The density contrast

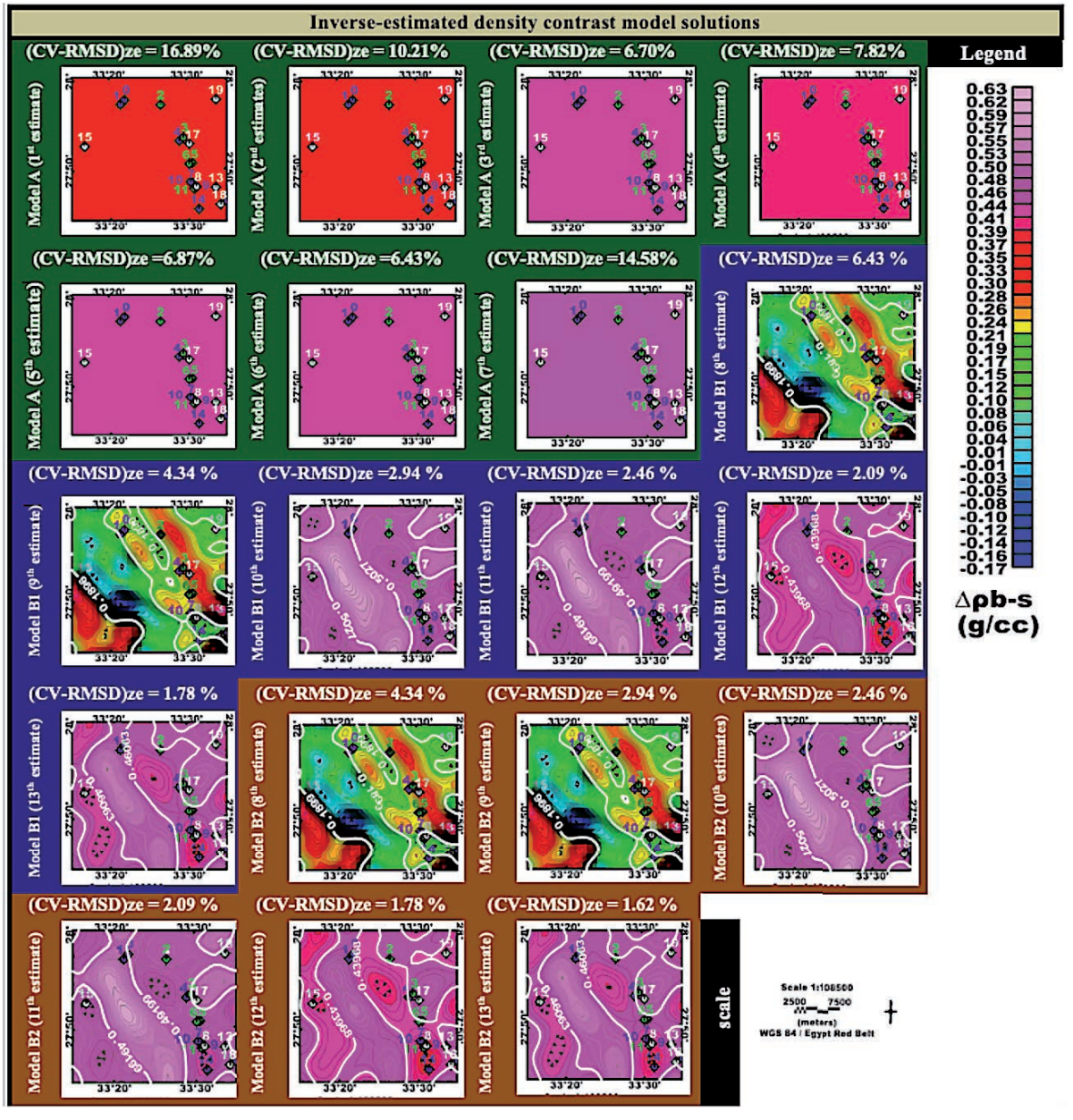

Figure 6. The three lateral density contrast stages of assumed *A* (on green), recovered *B*1 (on blue), and constrained *B*2 (on brown background) between the basement and sedimentary section. Based on basement depth root mean squares, the estimated density contrast constraining approach was utilized between stages two and three to figure out the optimal lateral density contrast between the basement and sediments, obtained at the thirteenth trial with a 1.62% coefficient of variance

Рисунок 6. Три стадии латерального контраста плотности: предполагаемый *A* (на зелёном), восстановленный *B*1 (на синем) и ограниченный *B*2 (на коричневом фоне) между фундаментом и разрезом осадочных пород. Согласно среднеквадратическим значениям глубины фундамента, подход к ограничению оценочного контраста плотности использовался между вторым и третьим этапами для определения оптимального латерального контраста плотности между фундаментом и отложениями, полученного в тринадцатой пробе с коэффициентом дисперсии 1,62 %

is laterally constrained within this range: 0.5458 – 0.3835 g/cc. An El-Zeit sedimentary-basement basinal depth model was developed using optimized density contrast parameters and their optimum constraint assumption at the interfaced surface with delineations mean error of 1.63%.

The Bouguer response of the optimal model was interpreted using the Δ*de* data-misfit parameters (Mean 0.0045, Max 14.2795, Min – 4.9724, and SD 1.3111 mGal). Thirteenth-estimate in (Figs 7, 8) show the lateral distribution of linear and normal-colored Bouguer anomalous misfits after recovering optimal inverse-estimated model solutions.

The color legend for fig. 8's thirteenth-estimate shows the minimum mean data misfit estimations of 0.0045 mGal, encompassing most of the study area between the estimated and observed Bouguer anomalies, with mean values of *de* = –24.9139 and *da* = –24.9094. The mean Bouguer anomaly misfit falls between –4.9724 and 14.2795 mGal.

Thirteenth-estimate in fig. 7 shows how two substantial normal faults and elongated basins in the sedimentary layer above the basement complex allowed oil to migrate from the El-Zeit central basin at high pressure and accumulate where these elongated basins are at low pressure. These Extended

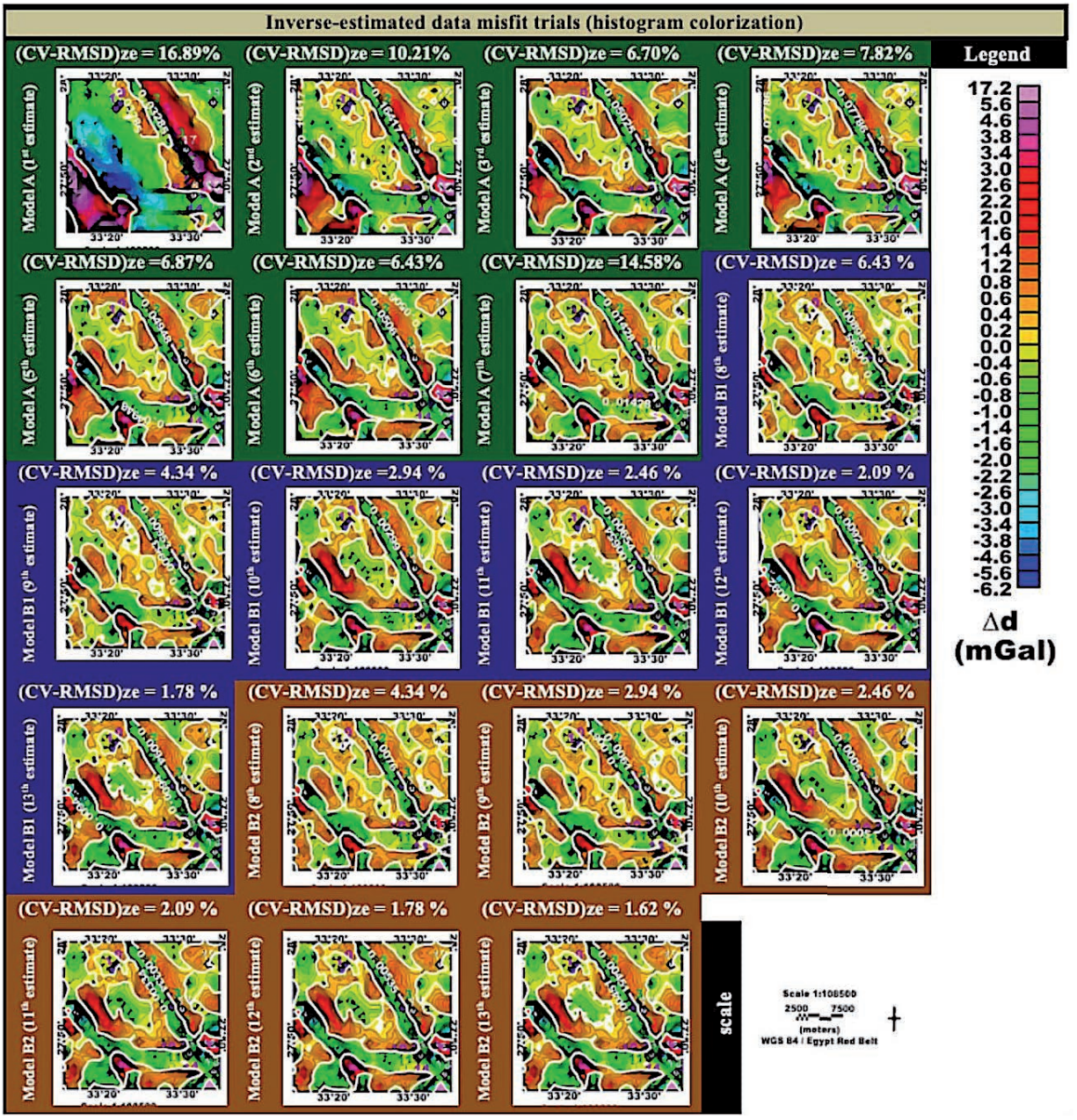

Figure 7. The three-stage optimization process of normally colored-estimated residual Bouguer anomaly gravity data produced an image limited by a 1.62% error in the depth of the sedimentary basinal structure above the basement complex, which formed the deep basin pattern in the study area of the Gebel El-Zeit area. Models *A*, *B*1, and *B*2 plot trials on green, blue, and brown backgrounds, respectively

Рисунок 7. Трехэтапный процесс оптимизации нормальных оцененных цветных остаточных гравитационных данных аномалии Буге позволил получить изображение, ограниченное ошибкой 1,62 % в глубине осадочной структуры бассейна над комплексом фундамента, что сформировало структуру глубокого бассейна в районе исследования Гебель-эль-Зейт. Модели *A*, *B*1 и *B*2 отображают пробы на зеленом, синем и коричневом фоне соответственно

basins cause low Bouguer anomalies, as revealed on the map of this thirteenth-estimate. The two principal normal faults of the Graben system compressed sedimentary strata over a basement complex to generate these basins. Middle El-Zeit fault compression creates subsidiary sedimentary basins.

The optimal model's minimal error solutions were achieved by imposing the following constraints on the third-last stage's inverse-estimated parameterization sequence: *DC* shift of 42.6709 mGal, filter LHC limit of 20 000 m, filter UHC limit of 15 000 m, convergence limit of 0.0001 mGal, and regional offset of 0 mGal. The first constraint parameter (*DC* shift = 42.6709 mGal) predicted the initial mean depth parameter (Mean DTB_0 = –3536 m) and the inverse mean depth (Mean *DTBe* = –3534.6 m). The second constraint parameter, which bounds the filter LHC to 20 000 m, smoothed the optimal inverse-estimated mean density-depth model and mean-Bouguer-anomaly response. The third constraint, which bounds filter UHC to 15 000 m, optimizes the second constraint. The second and third parameters determine model solution and data calculation detailedness and smoothness. The research area's optimal inverse model solutions fit estimated and observed Bouguer

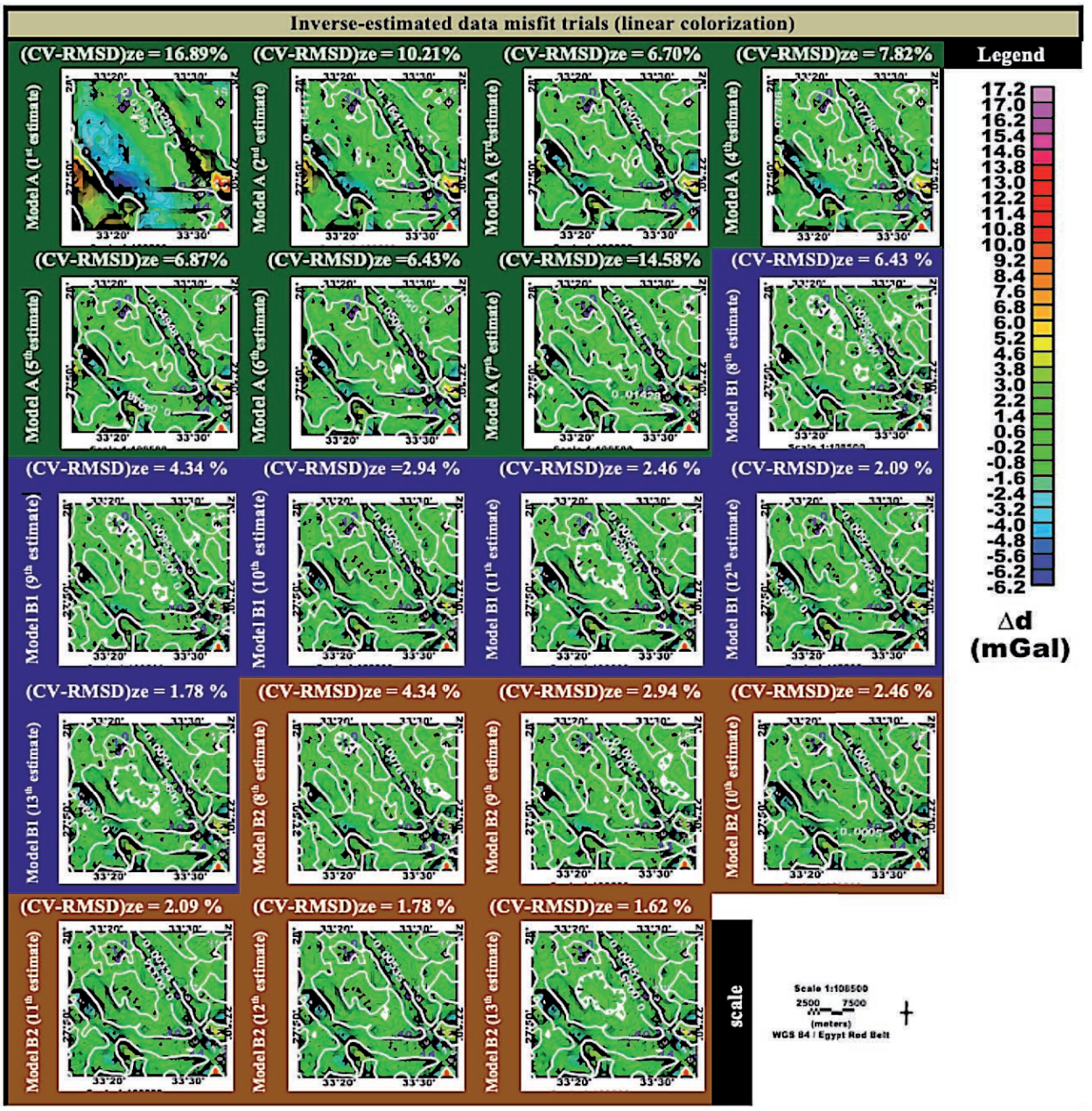

Figure 8. Linearly colored maps of residual Bouguer anomaly gravity data match the normal colorized-estimated maps, shown in fig. 5. These maps reflect the optimization with the constraining procedure of the three-stage inversion scheme's mean data misfit, yielding an optimal solution with a low root-mean-square coefficient of variance of 1.62%. Model *A* shows first-stage estimations on green, Model *B*1 on blue, and Model *B*2 on brown

Рисунок 8. Линейно раскрашенные карты остаточных гравитационных данных аномалии Буге соответствуют нормальным цветным оценочным картам, показанным на рис. 5. Эти карты отражают оптимизацию с помощью процедуры ограничения несоответствия средних данных трехэтапной схемы инверсии, что дает оптимальное решение с низким среднеквадратичным коэффициентом дисперсии 1,62 %. Модель *A* показывает оценки первого этапа зеленым цветом, модель *B*1 — синим, а модель *B*2 — коричневым

anomalies with a mean misfit of 0.0045 mGal. Zeroing the fourth regional offset constraint parameter accomplishes this. The inversion run ends when the fifth convergence limit parameter, 0.0001 mGal, reduces the standard deviation difference between the data misfit of the last two iterations. The fourth and fifth constraint parameters help compute the optimal inverse model solution with minimal computational errors.

Evaluation of the inversion stages

Quality control and indirect constraint at drilled wells`locations. Figs 9.1; 9.2 show the constraint wells utilized for quality control and testing the optimality of inversion solutions. Gravity inversion was used to determine the 3D basement depth using 19 wells in the research region. To reconcile calculated data and model solutions with observed values, the *DC* shift, convergence limit, regional offset, and filter's lower-upper high cut limits were adjusted. As the first quality control, six Basement constraint wells were used after inversion to check if the inverse depth values were within the analytical depth range. As a secondary quality control test, we checked if the optimal inverted basement

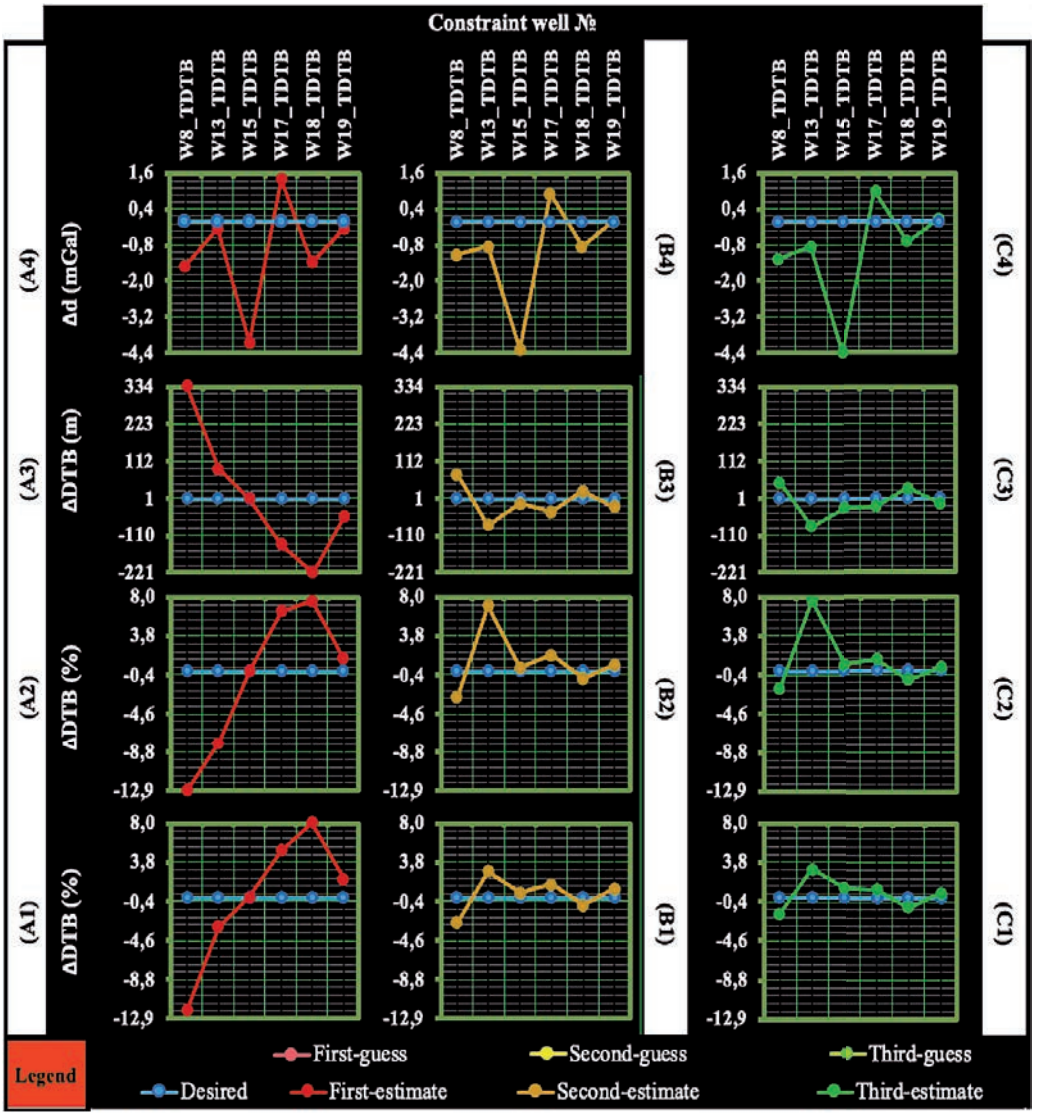

Figure 9.1. The optimality of a three-stage best-possible forward-guesses and inverse-estimates depth-density model solution analyzed for wells with a reachable total basement depth constraint, revealing the best indirect quality control test executed within the proposed inversion scheme

Рисунок 9.1. Оптимальность трехэтапного решения модели глубины–плотности с наилучшими возможными предположениями и обратными оценками, рассчитанными на скважины с достижимым ограничением общей глубины фундамента, выявила лучший тест косвенного контроля качества, выполненный в рамках предложенной схемы инверсии

depth surpassed the depth of the thirteen inaccessible basement constraint wells.

The first and second controls imply a forward-starting model with weak depth limitations and then invert the optimum 3D lateral depth solution with little error. This strategy works better with minimal prior knowledge and uses the recommended inversion method in a unique field that requires more data for reasonable projections.

Regarding the third quality control, this study compared computed and actual Bouguer anomalies at nineteen accessible control wells. A tertiary control test can obtain a mean data misfit near zero by halting inversion at regional null offsets. The depth-density model's optimal solution matches the scenario's minimal data misfit (Fig. 9.1, Graphs *A*4–*C*4, and fig. 9.2, Graphs *B* and *C*) support this claim.

In the fourth control test, we examined lateral basement density and the disparity between the basement and sedimentary densities to test our inversion scheme's density estimations. This work tested a lateral density model to optimize the density contrast between the basement and sedimentary layers and reduce basement depth estimation inaccuracy.

The graphs *A*3–*C*3 (Fig. 9.1) show that the sixth optimal inverse trial of the mean basement depth model had the lowest calculation error for the first stage of the proposed inversion scheme. The six constraint wells' actual and estimated depths related by first-stage optimality revealed this sequence of estimated depths of *W*8 – 2910.6, *W*13 – 1216.68, *W*15 – 3767, *W*17 – 2023.1, *W*18 – 2686.7, and *W*19 – 3995.3 m, misfitting with the actual depths by this misfit sequence of *W*8 – 333.6, *W*13 – 87.8, *W* – 15 2.0, *W*17 138.8, *W*18 221.2, and *W*19 55.7 m. Our third stage updated the basement depth model as follows: *W*8 – 2624, *W*13 – 1044.2, *W*15 – 3738.7, *W*17 – 2135.4, *W*18 – 2938.3, and *W*19 – 4035.5 m, resulting in the best correlation to the actual depths. Hence, the depth misfit sequence decreased considerably to be (*W*8 – 46.9, *W*13 84.7, *W*15 30.2, *W*17 26.5, *W*18 – 30.2, *W*19 15.4 m). The depth

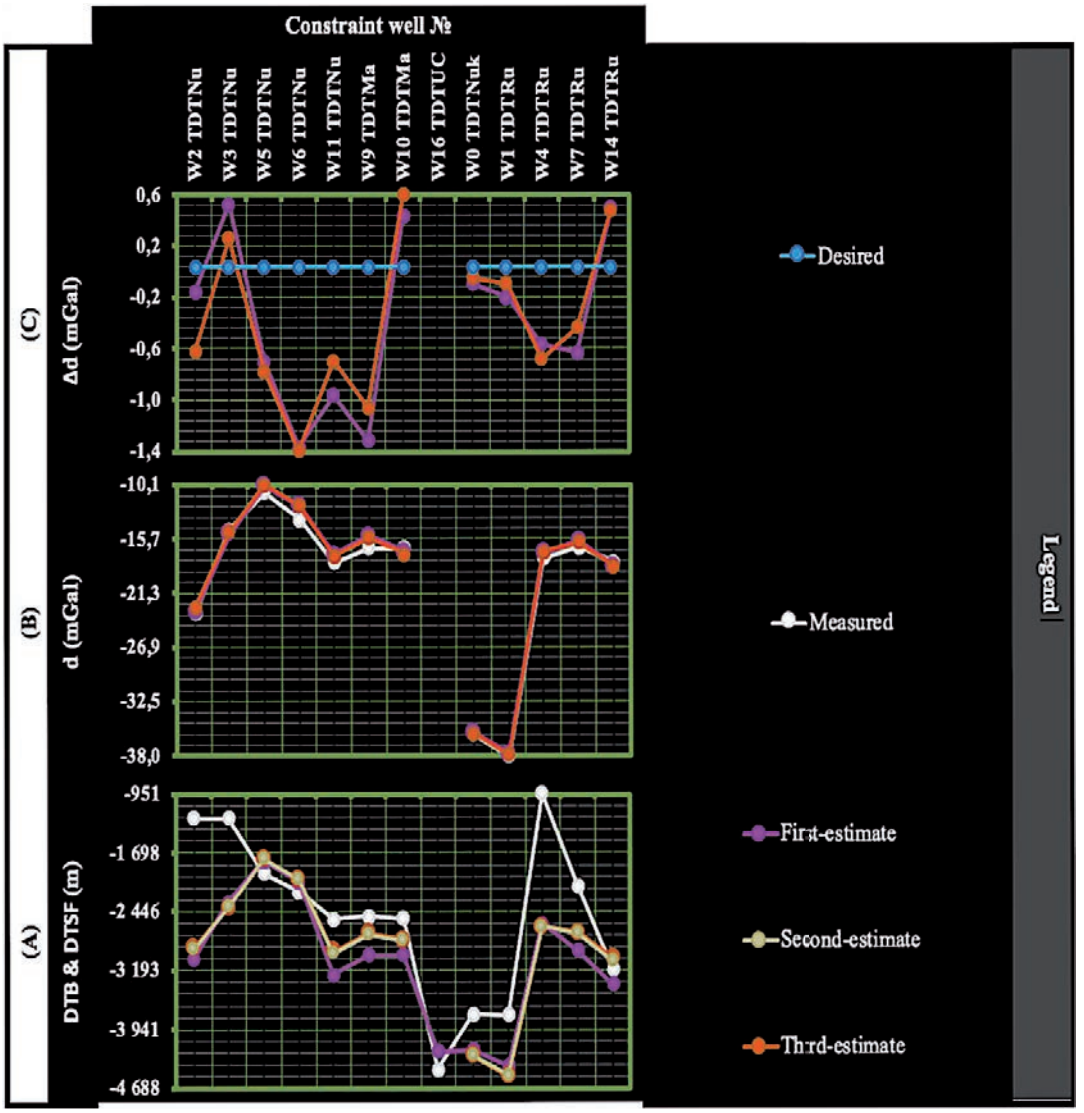

Figure 9.2. The indirect best quality control carried out on the inverse results of the proposed inversion scheme constrained by the minimal estimated data misfit (Graphs *A* and *B*) revealed by the inverse analysis of the three-stage best-possible basement depth model estimates for thirteen unreachable total depth basement constraint wells (graph *C*). A comprehensive list of abbreviations is provided in table 2

Рисунок 9.2. Косвенный контроль наилучшего качества осуществляется на основе обратных результатов предложенной схемы инверсии, ограниченной минимальным несоответствием расчетных данных (графики *А* и *Б*), выявленным в результате обратного анализа трехэтапных оценок модели наилучшей глубины фундамента для тринадцати недостижимых скважин с ограничением фундамента общей глубины (график *С*). Полный список сокращений представлен в табл. 2

misfit sequence shows that our third stage produces a more accurate optimal depth model.

Graphs *A*2–*C*2 in fig. 9.1 explains the sequencing-reestimated depth misfit percentages. The first stage's sixth optimal depth misfit trial resulted in a percentage inaccuracy sequence of *W*8 12.9, *W*13 7.7, *W*15 –0.05, *W*17 –6.4, *W*18 – 7.60, and *W*19 – 1.37 %, while the third stage had a percentage inaccuracy sequence of *W*8 1.8, *W*13 7.5, *W*15 0.8, *W*17 1.2, *W*18 1.0, and *W*19 – 0.4%.

Graphs *A*1–*C*1 in (Fig. 9.1) compares the re-estimated optimal depth misfit sequences to the mean basement depth of the six constraint wells. The graph shows well-specific percentage coefficients of variation. The first stage re-estimates the sixth optimal depth misfit sequence with estimates *W*8 12.0, *W*13 13.2, *W*15 – 0.07, *W*17 – 5.0, *W*18 – 7.9, and *W*19 – 2.0%, while the third stage re-estimates the sequence with estimates *W*8 1.7, *W*13 -3.0, *W*15 – 1.1, *W*17 – 0.9, *W*18 1.1, and *W*19 – 0.5%.

As shown in fig. 9.1, graph *C*2, the confined mean density trial was allocated among six controlled wells based on lateral density sequence with best-possible constrained densities of 2.617, 2.668, 2.634, 2.689, 2.665, and 2.661 g/cc at the constraint wells *W*8, *W*13, *W*15, *W*17, *W*18, and *W*19, respectively.

Fig. 9.2, graph *C*4 shows the six wells' data-misfit sequence between estimated and observed data (*W*8 –1.254, *W*13 – 0.856, *W*15 – 4.414, *W*17 1.000, *W*18 – 0.704, and *W*19 0.088 mGal), which reflects the optimality of the basement depth-density solution. Fig. 9.2, graph *C* shows that the data-misfit sequence (*W*2 – 0.6515, *W*3 0.2162, *W*5 – 0.8159, *W*6 – 1.4316, *W*11 – 0.7332, *W*9 – 1.0979, *W*10 0.5582, *W*0 – 0.0871, *W*1 – 0.1342, *W*4 – 0.7195, *W*7 – 0.4348 mGal) resulted in the basement optimal estimated depths being more profound than the actual depths of various sedimentary formations in the sedimentary section for the thirteen wells.

Fig. 10.1, Map *B* shows lines *A*-*A*', *B*-*B*', *C*-*C*', and *D*-*D*', indicating the asymmetrical basin's breadth along the

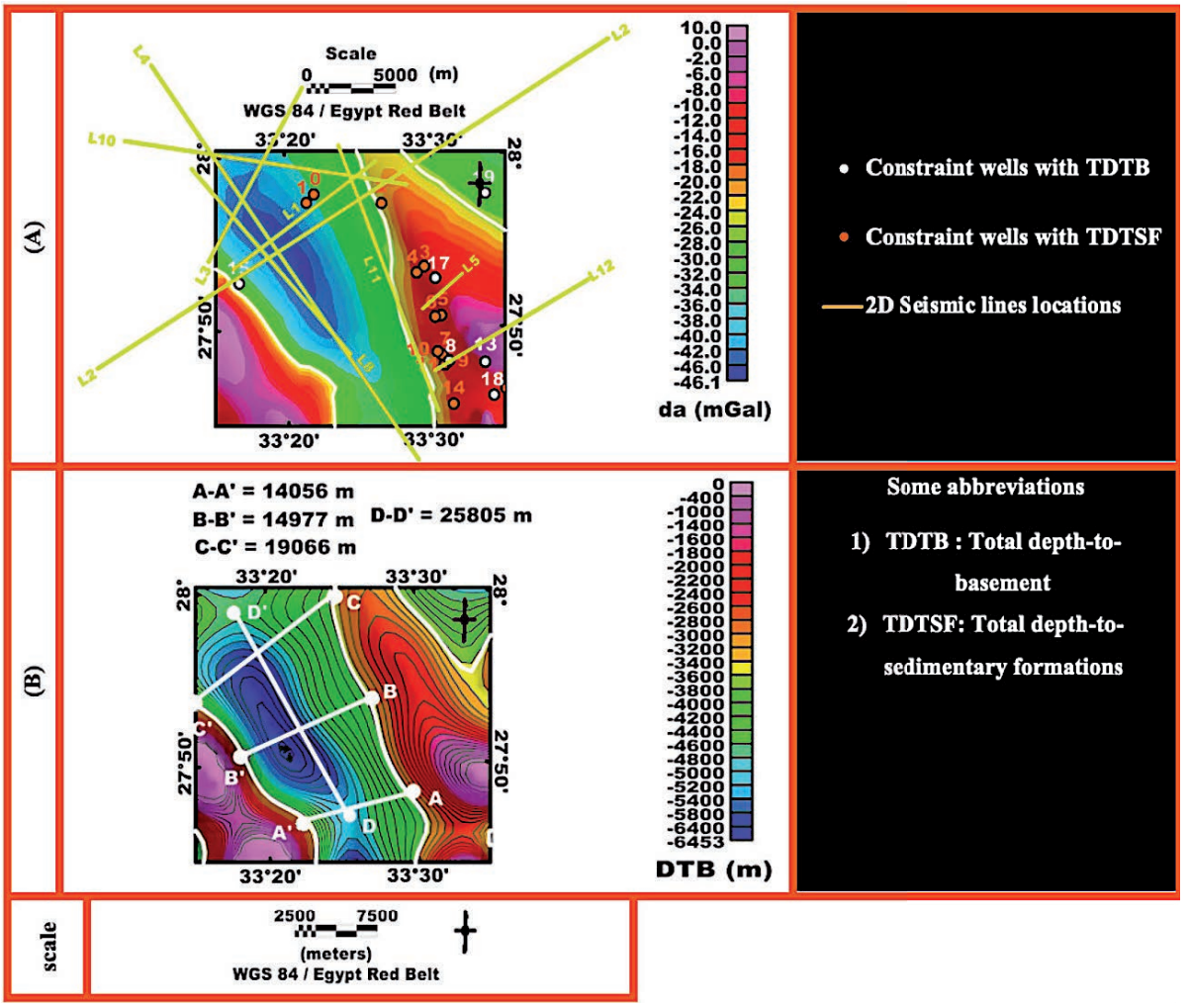

Figure 10.1. The study area's accessible seismic line sites, as shown on a map of Bouguer gravity data (*A*) and measurements of the El-Zeit basin's 1.62% roughly dimensions using mean depth white contour line as an indicator in the proposed inversion scheme's third-final stage optimal-inverse basement depth map (*B*)

Рисунок 10.1. Доступные участки сейсмических линий на территории исследования, как показано на карте гравитационных данных Буге (*A*) и измерений 1,62 % приблизительных размеров бассейна Эль-Зейт с использованием белой контурной линии средней глубины в качестве индикатора на третьем заключительном этапе предлагаемой схемы инверсии оптимально-обратной карты глубины фундамента (*B*)

northwest-southeast axis. These lines are 25805 m long and 14 056, 14 977, and 19 066 m wide. The southern, middle, and northern basin widths are estimated. The appropriate sedimentary basin depth model can be produced by identifying the basement relief.

Quality control thru extraction of 2D gravity models at seismic lines' locations. Our fifth quality control test used a 3D gravity inverse optimal depth-density model solution to create 2D gravity model cross sections at 2D seismic line sites (Fig. 10.2) to show the basement relief of the El Zeit basin. (Fig. 10.3) show minimal Bouguer misfits resulting from the 2D optimal solutions of the density contrast interface between the basement and sedimentary layers (Figs 10.4) and the basement depth and basement complex's lateral density distribution (Fig. 10.5).

Figs 10.2–10.6 show 2D gravity inversion results for 13 seismic lines. The sixth trial in the inverse parameterization sequence of the inversion scheme's third-final stage yielded the optimal three-dimensional depth-density-gravity model for the study area. Inverse modeling yielded the best extracted two-dimensional gravity models from this model with minimal calculated inverse data misfit error, validating the optimal key parameter values of the 2D extracted model.

Conclusions

This study presents a multi-dimensional three-stage gravity inversion scheme for the southwestern part of the Gulf of Suez at the Gebel Zeit study area. The scheme incorporates three techniques involving different forward and inverse modeling scenarios. The optimization procedure focuses on parameterizing the forward modeling constrained by gradual decreased mean depth error initial guesses and optimizing inverse modeling estimates through multiple trials. The main objective is to obtain optimal solutions for the three-dimensional depth-density model, specifically the depth-to-basement, lateral density distribution of the basement complex, and lateral density contrast at the basement-sedimentary interface.

The starting three-dimensional forward depth-density models were initially built up with different guesses of

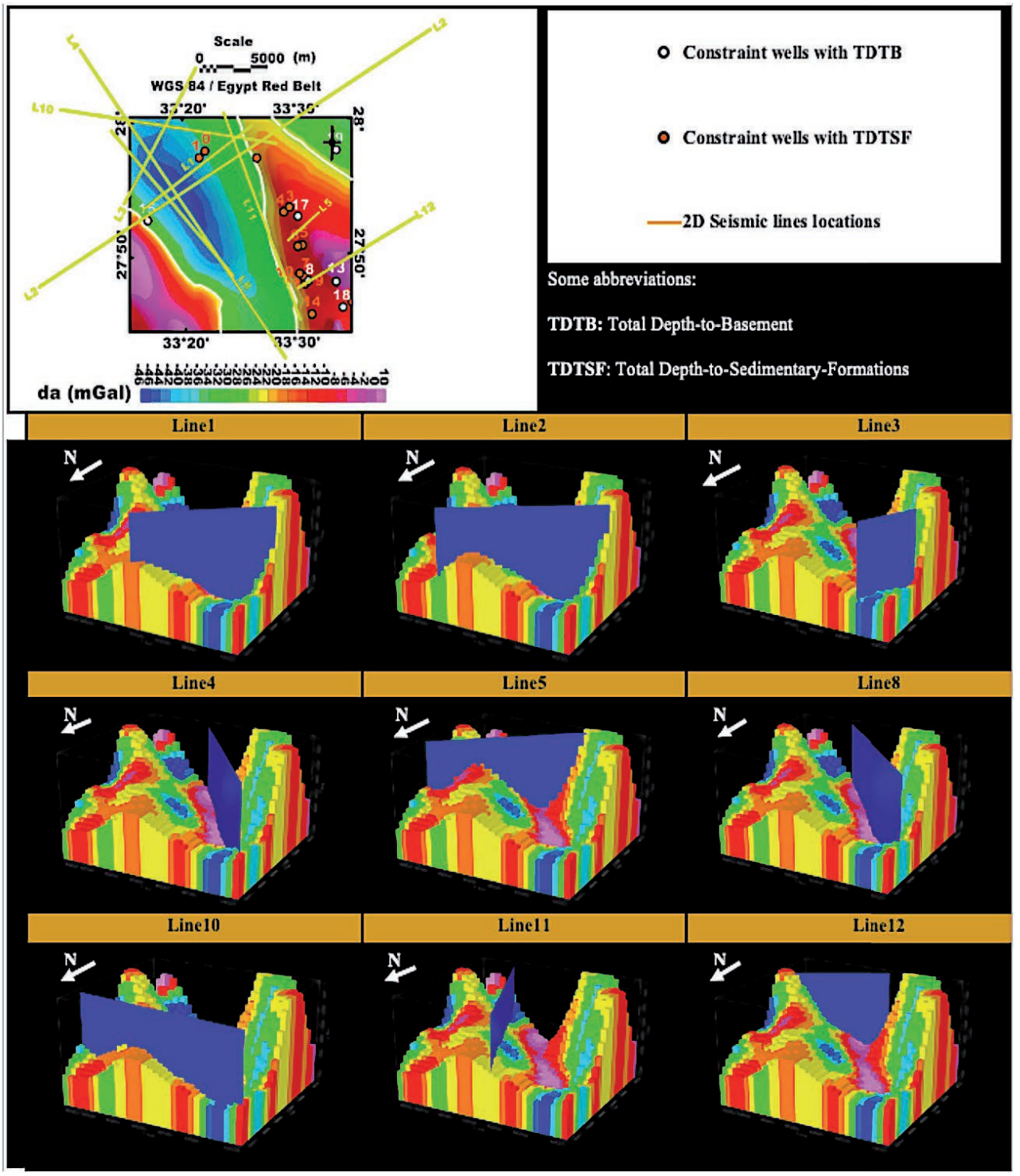

Figure 10.2 (continued in fig. 10.3)
Рисунок 10.2 (продолжение на рис. 10.3)

assumptions of using unconstrained even depth surfaces and constrained homogenous two-layered density trials, then using constrained uneven depth surfaces and unconstrained homogenous two-layered density trials, and finally using unconstrained uneven depth surfaces and constrained heterogenous two-layered density trials. The root-mean-square depth error coefficient of variance was initially guessed according to prior information about the actual basement mean depth gained from six reachable basement constraint wells accessible in the study area and constrained to be gradually decreasing through the three-stage forward modeling's creation sequence in the scheme. The forward and inverse parameterization sequences of the three techniques used were correlated within data analysis, reflecting the overall optimality of the scheme in decreasing the first-stage 56.9% starting error in forward modeling's initiation process to the third-stage 1.63% minimal estimated error in inverse modeling's recovery process.

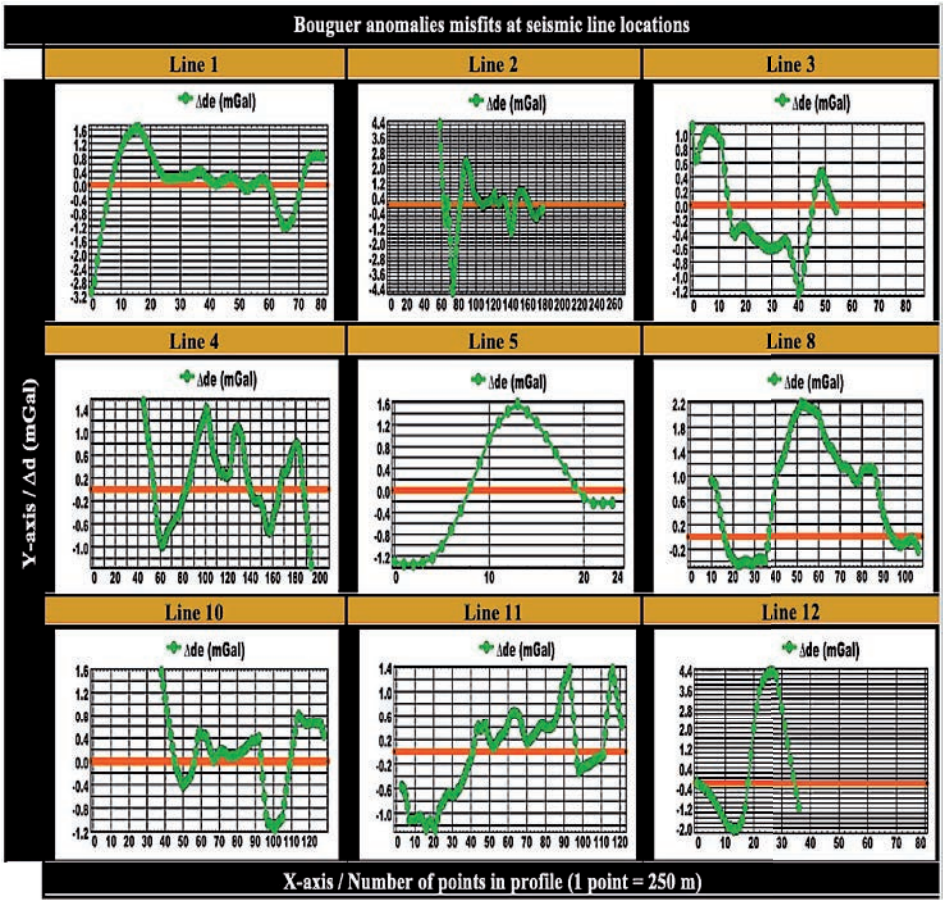

Figure 10.3 (continuation of fig. 10.2, continued in fig. 10.4)
Рисунок 10.3 (продолжение рис. 10.2, продолжение на рис. 10.4)

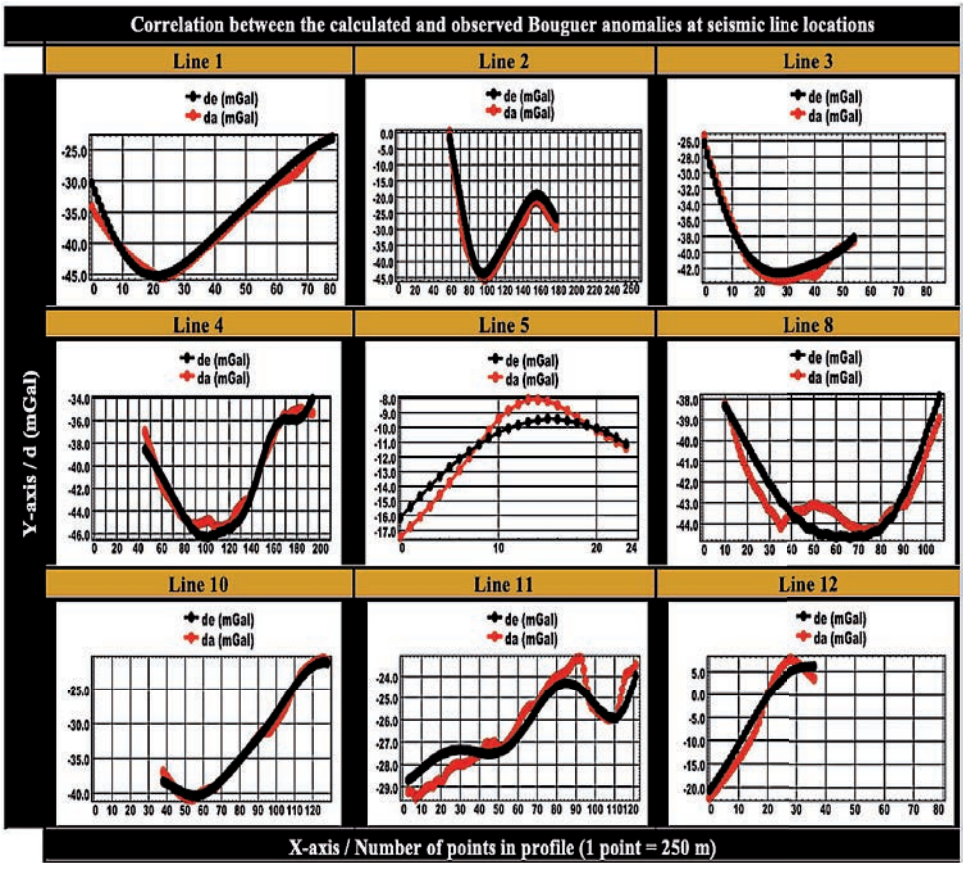

Figure 10.4 (continuation of fig. 10.3, continued in fig. 10.5)
Рисунок 10.4 (продолжение рис. 10.3, продолжение на рис. 10.5)

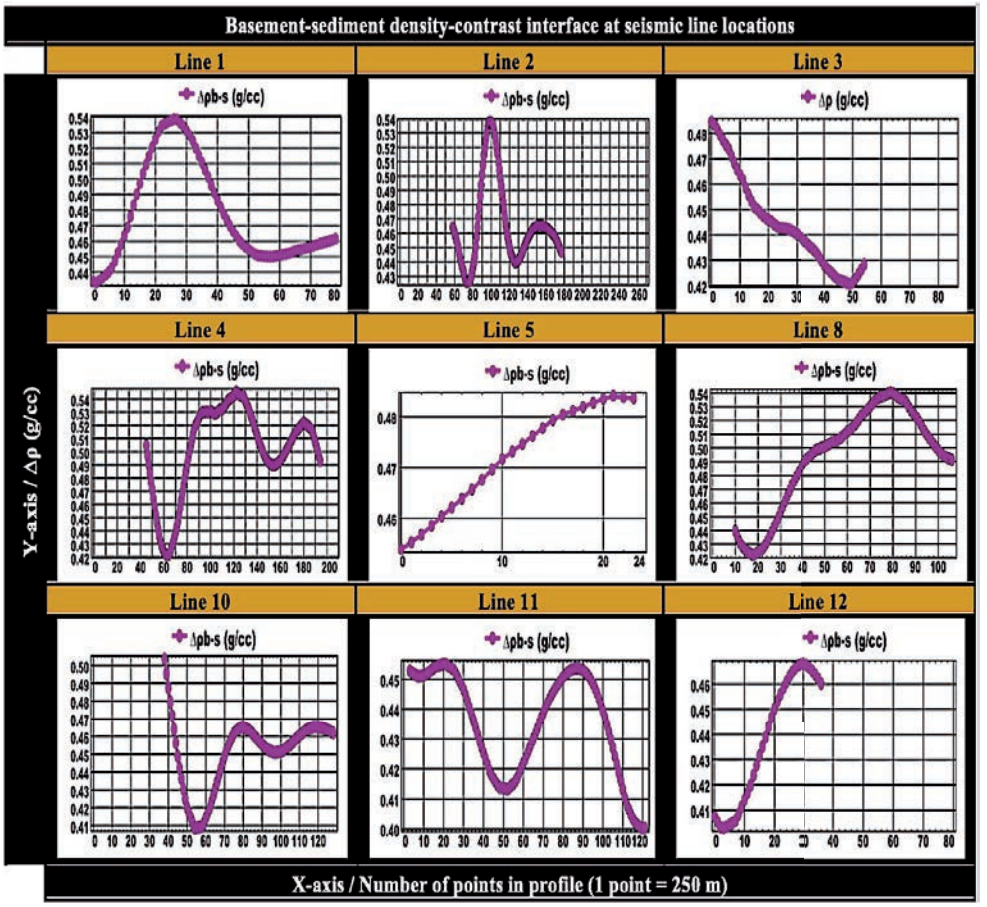

Figure 10.5 (continuation of fig. 10.4, continued in fig. 10.6)
Рисунок 10.5 (продолжение рис. 10.4, продолжение на рис. 10.6)

The study aimed to improve the scheme's credibility for future recommendations in new places with inadequate data and prior information. Refining the scheme yielded optimized depth-density model solutions that correlated best with geological data and minimized error estimates. The study employed a scheme parameterization strategy that followed the inversion process constraint of *DC* shift instead of the direct constraint of the accessible wells, balancing initial guesses with inverse estimates. The zero-regional offset requirement minimized residual estimated Bouguer gravity data misfit and aids inverse model recovery.

After conducting a depth inversion procedure using three forwardly modeled scenarios and a density inversion procedure using additional three forwardly modeled scenarios, the optimal basement depth in the area ranged between 0 and 6500 m from sea level. The predicted basement relief in the research region was depicted with a basinal structure in the central area and a basement complex lateral density model was recovered with densities ranging from 2.6706 to 2.7558 g/cc with a mean of 2.6706 g/cc for a 3534 m mean basement depth recovered with error of 1.63%.

The study assessed the effectiveness of recovering the 3D depth-density model at nine seismic lines, helping to identify the basement relief in the region, which is obscured in 2D seismic interpretation due to salt diapers. The fully recovered optimal three-dimensional image of the deep sedimentary structure above the basement relief in the research area provided valuable geological insights.

Acknowledgments

The researcher Ahmed G. M. Hassan, appreciates the financial support given to him by the Arabic Republic of Egypt, represented in the central department of Missions under the Cultural Affairs and Missions Sector at the Ministry of Higher Education of Egypt, covering his living expenses along with his study in Saint Petersburg State University in Russia. Also, he appreciates the chance given to him by the Russian Federation side, represented by the Russian Ministry of higher education, to be enrolled in a Ph.D. Program by a scholarship without payment of the education fees.

Authorship contributions

Ahmed G. M. Hassan: Conceptualization, methodology, software, formal analysis, validation, resources, writing – original draft preparation. Karam S. I. Farag: formal analysis, writing – review and editing, visualization. ALaa A. F. Aref: supervision. Alexey L. Piskarev: supervision. All authors have read and agreed to the published version of the manuscript.

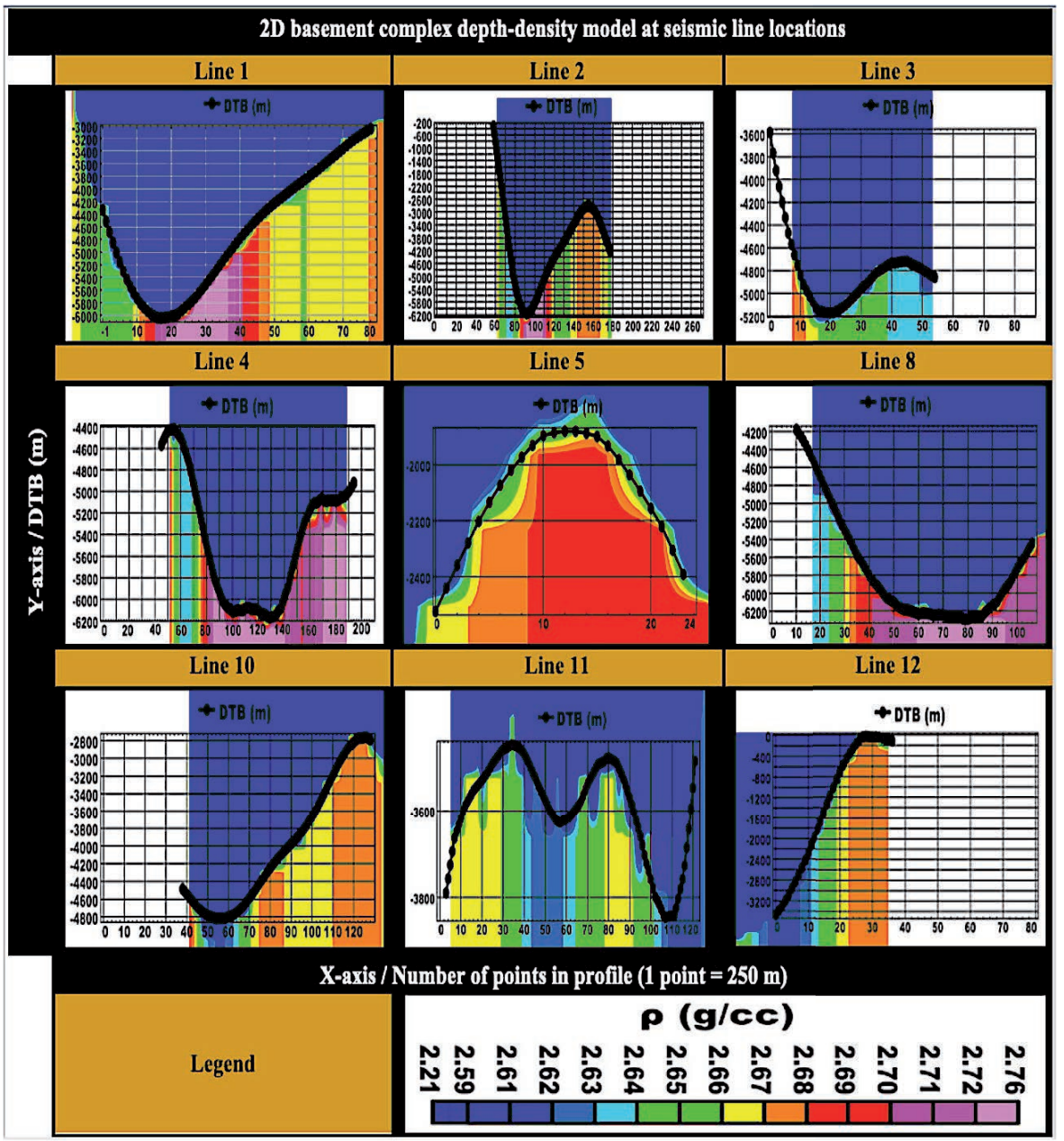

Figure 10.6. The continuation of figs 10.1, 10.2, 10.3, and 10.4, which together display the third-final stage optimality of the proposed inversion scheme in demonstrating the best quality control in extracting 2D basement depth-density model solutions from 3D inverted basement complex gravity model solutions with minimal Bouguer gravity data misfit at nine seismic lines

Рисунок 10.6. Продолжение рис. 10.1, 10.2, 10.3 и 10.4, которые вместе демонстрируют оптимальность третьего заключительного этапа предлагаемой схемы инверсии при демонстрации наилучшего контроля качества при извлечении решений 2D-модели глубины и плотности фундамента из 3D-решений инвертированной сложной гравитационной модели фундамента с минимальным несоответствием данных гравитации Буге на девяти сейсмических профилях

Disclosure of Funding Sources

The researcher Ahmed G. M. Hassan is funded by a scholarship [EGY-6958/16] under the joint executive program between Arab republic of Egypt and Russia

Declaration of Competing Interest

The authors declare that they have no known competing financial interests or personal relationships that could have appeared to influence the work reported in this paper.

REFERENCES

1. Jessell M. et al. 2014, Next Generation Three-Dimensional Geologic Modeling and Inversion. Building Exploration Capability for the 21st Century. Karen D. Kelley, Howard C. Golden (eds). Littleton, Colorado, USA: Society of Economic Geologists, Inc., ch. 13, pp. 261–272. https://doi.org/10.5382/SP.18.13

2. Fan D., Li S., Li X., Yang J., Wan X. 2021, Seafloor Topography Estimation from Gravity Anomaly and Vertical Gravity Gradient Using Nonlinear Iterative Least Square Method. *Remote Sensing*, vol. 13, pp. 1–19. https://doi.org/10.3390/rs13010064

3. Silva J. B. C., Santos D. F., Gomes K. P. 2014, Fast gravity inversion of basement relief. *Geophysics*, vol. 79, issue 5, pp. G79–G91. https://doi.org/10.1190/GEO2014-0024.1
4. Pham L. T., Oksum E., Do T. D. 2018, GCH_gravinv: A MATLAB-based program for inverting gravity anomalies over sedimentary basins. *Computers & Geosciences*, vol. 120, pp. 40–47. https://doi.org/10.1016/j.cageo.2018.07.009
5. Cremon M., Burnham A. K., Liu Y., Lapene A. 2017, Modified Athy-Law Compaction to Account for Porosity Generation and Preservation from Kerogen Conversion in Terzaghi-Like Models of Petroleum Source Rocks. AAPG Annual Convention & Exhibition, Houston, Texas, April 2–5, 2017, article number 42062, pp. 1–18.
6. Wu L. 2018, Efficient Modeling of Gravity Fields Caused by Sources with Arbitrary Geometry and Arbitrary Density Distribution. *Surveys in Geophysics*, vol. 39, issue 3, pp. 401–434. https://doi.org/10.1007/s10712-018-9461-7
7. Santos D. F., Silva J. B. C., Martins C. M., Santos R. C. S., Ramos L. C., Araújo A. C. M. 2015, Efficient gravity inversion of discontinuous basement relief. *Geophysics*, vol. 80, issue 4, pp. G95–G106. https://doi.org/10.1190/geo2014-0513.1
8. Preston L., Poppeliers C., Schodt D. J. 2020, Seismic Characterization of the Nevada National Security Site Using Joint Body Wave, Surface Wave, and Gravity Inversion. *Bulletin of the Seismological Society of America*, vol. 110, issue 1, pp. 110–126.
9. Wu L. 2016, Efficient modelling of gravity effects due to topographic masses using the Gauss–FFT method. *Geophysical Journal International*, vol. 205, no. 1, pp. 160–178. https://doi.org/10.1093/gji/ggw010
10. Wu L., Lin Q. 2017, Improved Parker's method for topographic models using Chebyshev series and low rank approximation. *Geophysical Journal International*, vol. 209, issue 2, pp. 1296–1325. https://doi.org/10.1093/gji/ggx093
11. Wu L. 2019, Fourier-domain modeling of gravity effects caused by polyhedral bodies. *Journal of Geodesy*, vol. 93, no. 5, pp. 635–653.
12. Mallesh K., Chakravarthi V., Ramamma B. 2019, 3D Gravity Analysis in the Spatial Domain: Model Simulation by Multiple Polygonal Cross-Sections Coupled with Exponential Density Contrast. *Pure and Applied Geophysics*, vol. 176, issue 5, pp. 2497–2511. https://doi.org/10.1007/s00024-019-02103-9
13. Stolk W., Kaban V., Beekman F., Tesauro M., Mooney W. D., Cloetingh S. 2013, High resolution regional crustal models from irregularly distributed data: Application to Asia and adjacent areas. *Tectonophysics*, vol. 602, pp. 55–68. https://doi.org/10.1016/j.tecto.2013.01.022
14. Buccini A. 2016, Tikhonov-type iterative regularization methods for ill-posed inverse problems: theoretical aspects and applications. PhD thesis. Varese, Italy: University of Insubria.
15. Dadak B. 2017, Inversion of gravity data for depth-to-basement estimate using the volume and surface integral methods: model and case study. Salt Lake City, Utah, USA: The University of Utah, 84 p.
16. Maag E., Li Y. 2018, Discrete-valued gravity inversion using the guided fuzzy *c*-means clustering technique. *Geophysics*, vol. 83, issue 4, pp. 59–77. https://doi.org/10.1190/geo2017-0594.1
17. Feng X., Wang W., Yuan B. 2018, 3D gravity inversion of basement relief for a rift basin based on combined multinorm and normalized vertical derivative of the total horizontal derivative techniques. *Geophysics*, vol. 83, issue 5, pp. G107–G118. https://doi.org/10.1190/geo2017-0678.1
18. Cella F., Nappi R., Paoletti V., Florio G. 2021, Basement Mapping of the Fucino Basin in Central Italy by ITRESC Modeling of Gravity Data. *Geosciences*, vol. 11, pp. 1–25. https://doi.org/10.3390/geosciences11100398
19. Ren Z., Chen C., Pan K., Kalscheuer T., Maurer H., Tang J. 2017, Gravity Anomalies of Arbitrary 3D Polyhedral Bodies with Horizontal and Vertical Mass Contrasts. Surveys in Geophysics, vol. 38, issue 2, pp. 479–502. https://doi.org/10.1007/s10712-016-9395-x
20. Vatankhah S., Renaut R. A., Huang X., Mickus K., Gharloghi M. 2022, Large-scale focusing joint inversion of gravity and magnetic data with Gramian constraint. *Geophysical Journal International*, vol. 230, issue 3, pp. 1585–1611. https://doi.org/10.1093/gji/ggac138
21. Makled W. A., Ashwah A. A. E. E., Lotfy M. M., Hegazey R. M. 2020, Anatomy of the organic carbon related to the Miocene syn-rift dysoxia of the Rudeis Formation based on foraminiferal indicators and palynofacies analysis in the Gulf of Suez, Egypt. *Marine and Petroleum Geology*, vol. 111, pp. 695–719. https://doi.org/10.1016/j.marpetgeo.2019.08.048
22. Abuzied S. M., Kaiser M. F., Shendi E.-A. H., Abdel-Fattah M. I. 2020, Multi-criteria decision support for geothermal resources exploration based on remote sensing, GIS and geophysical techniques along the Gulf of Suez coastal area, Egypt. *Geothermics*, vol. 88, article number 101893. https://doi.org/10.1016/j.geothermics.2020.101893
23. Bendaoud A., Hamimi Z., Hamoudi M., Djemai S., Zoheir B. 2019, The Geology of the Arab World – An Overview. Cham: Springer, 552 p. https://doi.org/10.1007/978-3-319-96794-3
24. Temraz M., Dypvik H. 2018, The Lower Miocene Nukhul Formation (Gulf of Suez, Egypt): microfacies and reservoir characteristics. *Journal of Petroleum Exploration and Production Technology*, vol. 8, no. 1, pp. 85–98. http://dx.doi.org/10.1007/s13202-017-0386-3
25. Van Dijk J., AlBloushi A., Ajayi A. T., De Vincenzi L., Ellen H., Guney H., Holloway P., Khdhaouria M., Mcleod I. S. 2019, Hydrocarbon exploration and production potential of the gulf of Suez basin in the framework of the new tectonostratigraphic model. SPE Gas & Oil Technology Showcase and Conference, Dubai, UAE, October 2019. https://doi.org/10.2118/198622-MS
26. Attia I., Helal I., El Dakhakhny A., Aly S. A. 2017, Using sequence stratigraphic approaches in a highly tectonic area: Case study – Nubia (A) sandstone in southwestern Gulf of Suez, Egypt. *Journal of African Earth Sciences*, vol. 136, pp. 10–21. https://doi.org/10.1016/j.jafrearsci.2017.06.001
27. Farouk S., Sen S., Pigott J., Sarhan M. A. 2022, Reservoir characterization of the middle Miocene Kareem sandstones, Southern Gulf of Suez Basin, Egypt. *Geomechanics and Geophysics for Geo-Energy and Geo-Resources*, vol. 8, pp. 1–17. https://doi.org/10.1007/s40948-022-00437-8
28. Embabi A., Abdelwahhab M., Abdelhafez N. 2021, Reservoir characterization and petroleum geology at Esh El Mallaha Field, southern gulf of Suez, Egypt. *Al-Azhar Bulletin of Science*. vol. 32, no. 2, pp. 1–12. https://doi.org/10.21608/absb.2021.89127.1130
29. Hadad Y. T., Hakimi M. H., Abdullah W. H., Kinawy M., El Mahdy O., Lashin A. 2021, Organic geochemical characteristics of Zeit source rock from Red Sea Basin and their contribution to organic matter enrichment and hydrocarbon generation potential. *Journal of African Earth Sciences*, vol. 177, article number 104151. https://doi.org/10.1016/j.jafrearsci.2021.104151
30. Said R. 2017, The geology of Egypt. 1st ed. Regional Geology Reviews. London, 734 p. https://doi.org/10.1201/9780203736678
31. Almalki K. A., Mahmud S. A. 2018, Gulfs of Suez and Aqaba: New insights from recent satellite-marine potential field data. *Journal of African Earth Sciences*, vol. 137, pp. 116–132. https://doi.org/10.1016/j.jafrearsci.2017.10.004
32. Afifi A. S., Moustafa A. R., Helmy H. M. 2016, Fault block rotation and footwall erosion in the southern Suez rift: Implications for hydrocarbon exploration. *Marine and Petroleum Geology*, vol. 76, pp. 377–396. https://doi.org/10.1016/j.marpetgeo.2016.05.029
33. Youssef M., El-Sorogy A., El-Sabrouty M., Al-Otaibi N. 2016, Invertebrate shells as pollution bio-indicators, Gebel El-Zeit area, Gulf of Suez. Egypt. *Indian Journal of Geo-Marine Sciences*, vol. 45, no. 5, pp. 687–695.
34. 2016, Ministry of Petroleum and Mineral Resources. Ganoub El-Wadi Petroleum Holding Company "Ganope". International Bid Round 2016, 1–7 p.
35. South H. [et al.]. 2009, The Source for Critical information and insight. Global Exploration & production service, Gulf of Suez south, Egypt. Status of Carto Data and IRIS21 databases, 1 p.
36. Aboud E., Salem A., Ushijima K. 2005, Subsurface structural mapping of Gebel El-Zeit area, Gulf of Suez, Egypt using aeromagnetic data. *Earth, Planets and Space*, vol. 57, pp. 755–760. https://doi.org/10.1186/BF03351854

The article was received on November 08, 2023

УДК 550.3+550.839+550.8.056+550.8.053 http://doi.org/10.21440/2307-2091-2024-1-7-32

Интеграция гравиметрических и скважинных данных для визуализации глубины и плотности трехмерной обратной модели глубинной структуры сложного фундамента, а также тектонических данных для дальнейшей разведки углеводородов в районе бассейна Эль-Зейт, юго-запад Суэцкого залива, Египет

Ахмед Гамаль Мохамед ХАССАН[1,2]
Карам Самир Ибрагим ФАРАГ[3]
Алаа Ахмед Фахми АРЕФ[2]
Алексей Лазаревич ПИСКАРЕВ[1]

[1]Санкт-Петербургский государственный университет, Санкт-Петербург, Россия
[2]Управление по ядерным материалам (УЯМ), Каир, Египет
[3]Университет Айн-Шамс, Каир, Египет

Аннотация

Актуальность работы. Соляные диапиры в осадочных толщах создают проблемы при интерпретации сейсмических данных в исследуемом регионе, тем самым препятствуя построению комплексной трёхмерной структуры центрального бассейна. Использование гравиметрических данных для исследования структуры блоков разломов фундамента, подстилающих осадочный бассейн в бассейне Гебель-эль-Зейт, расположенном в юго-западной части Суэцкого залива в Египте, считается настоятельно рекомендуемым методом для получения тектонических данных с целью изучения углеводородов в этой области.

Методы исследования. В настоящем исследовании используются гравитационные аномалии Буге для включения допущений модели латеральной плотности фундаментного комплекса с целью определения наилучшей трехмерной глубины фундамента для рассматриваемой территории. Предлагаемая методология использует последовательные методы трехмерной спектральной инверсии слоистой среды. Различные методологии прямой оптимизации и последовательности параметризации были протестированы с помощью Ольденбургской и других прямых моделей в процессе интеграции различных предположений о параметрах ограничений для управления процедурами инверсии.

Результаты и выводы. Предлагаемая трехэтапная схема гравитационной инверсии предназначена для обнаружения оптимального решения по глубине и плотности при минимизации несоответствия расчетных данных в максимально возможной степени. Путем определения соответствующих параметров для решения трехмерной модели глубины и плотности настоящее исследование применяет статистический анализ для определения рельефа фундамента и его сложного латерального распределения плотности. При нулевом региональном смещении гравитации и постоянном сдвиге не было выявлено срединной ошибки, что позволило оптимально ограничить модель латеральной плотности. Сопоставление данных по глубинам нескольких скважин стратиграфического контроля, пробуренных в инвертированной 3D-модели фундамента, продемонстрировало оптимальность рельефа фундамента на изучаемой территории. Результаты корреляционного анализа показывают, что ожидаемая и измеренная глубины наиболее соответствуют друг другу. Такая аппроксимация означает, что оптимально принимается латеральное распределение плотности комплекса фундамента, что приводит к минимальной ошибке расчета по глубине и указывает на высокую тектонику исследуемой территории и высокую вероятность захвата углеводородов.

Ключевые слова: Египет, Суэцкий залив, район бассейна Эль-Зейт, аномалии Буге, схема спектрально-слоистой гравитационной инверсии, параметризация и оптимизация.

Благодарности

Исследователь Ахмед Г. М. Хассан благодарен за финансовую поддержку, оказанную ему Арабской Республикой Египет, представленной в центральном отделе миссий при отделе по делам культуры и миссионерскому сектору Министерства высшего образования Египта, покрывающую его расходы на проживание во время учебы в Санкт-Петербургском государственном университете в России. Также он ценит возможность, предоставленную ему Российской

✉ahmed.gamal_88@hotmail.com

Федерацией в лице Министерства высшего образования России, поступления в аспирантуру. Программа по стипендии без оплаты за обучение.

Авторский вклад

Ахмед Г. М. Хассан: концептуализация, методология, программное обеспечение, формальный анализ, проверка, ресурсы, написание – подготовка оригинального проекта. Карам С. И. Фараг: формальный анализ, написание – рецензирование и редактирование, визуализация. Алаа А. Ф. Ареф: кураторство. Алексей Леонидович Пискарев: авторский надзор. Все авторы прочитали и согласились с опубликованной версией рукописи.

Раскрытие источников финансирования

Исследователь Ахмед Г. М. Хассан финансируется за счет стипендии [EGY-6958/16] в рамках совместной исполнительной программы Арабской Республики Египет и России.

Декларация о конкурирующих интересах

Авторы заявляют, что у них нет известных конкурирующих финансовых интересов или личных отношений, которые могли бы повлиять на работу, представленную в этой статье.

ЛИТЕРАТУРА

1. Jessell M. et al. Next Generation Three-Dimensional Geologic Modeling and Inversion. Building Exploration Capability for the 21st Century. Chapter 13. Karen D. Kelley and Howard C. Golden (eds). Littleton, Colorado, USA: Society of Economic Geologists, 2014. P. 261–272. https://doi.org/10.5382/SP.18.13
2. Fan D., Li S., Li X., Yang J., Wan X. Seafloor Topography Estimation from Gravity Anomaly and Vertical Gravity Gradient Using Nonlinear Iterative Least Square Method // Remote Sensing. 2021. Vol. 13. P. 1–19. https://doi.org/10.3390/rs13010064
3. Silva J. B. C., Santos D. F., Gomes K. P. Fast gravity inversion of basement relief // Geophysics. 2014. Vol. 79. No. 5. P. G79–G91. https://doi.org/10.1190/geo2014-0024.1
4. Pham L. T., Oksum E., Do T. D. GCH_gravinv: A MATLAB-based program for inverting gravity anomalies over sedimentary basins // Computers & Geosciences. 2018. Vol. 120. P. 40–47. https://doi.org/10.1016/j.cageo.2018.07.009
5. Cremon M., Burnham A. K., Liu Y., Lapene A. Modified Athy-Law Compaction to Account for Porosity Generation and Preservation from Kerogen Conversion in Terzaghi-Like Models of Petroleum Source Rocks // AAPG Annual Convention and Exhibition. 2017. Article number 42062. P. 1–18.
6. Wu L. Efficient Modeling of Gravity Fields Caused by Sources with Arbitrary Geometry and Arbitrary Density Distribution // Surveys in Geophysics. 2018. Vol. 39. Issue 3. P. 401–434. https://doi.org/10.1007/s10712-018-9461-7
7. Santos D. F., Silva J. B. C., Martins C. M., Santos R. C. S., Ramos L. C., de Araújo A. C. M. Efficient gravity inversion of discontinuous basement relief // Geophysics. 2015. Vol. 80. No. 4. P. G95–G106. https://doi.org/10.1190/geo2014-0513.1
8. Preston L., Poppeliers C., Schodt D. J. Seismic Characterization of the Nevada National Security Site Using Joint Body Wave, Surface Wave, and Gravity Inversion // Bulletin of The Seismological Society of America. 2020. Vol. 110. No. 1. P. 110–126. http://dx.doi.org/10.1785/0120190151
9. Wu L. Efficient modelling of gravity effects due to topographic masses using the Gauss–FFT method // Geophysical Journal International. 2016. Vol. 205. Issue 1. P. 160–178. https://doi.org/10.1093/gji/ggw010
10. Wu L., Lin Q. Improved Parker's method for topographic models using Chebyshev series and low rank approximation // Geophysical Journal International. 2017. Vol. 209. Issue 2. P. 1296–1325. https://doi.org/10.1093/gji/ggx093
11. Wu L. Fourier-domain modeling of gravity effects caused by polyhedral bodies // Journal Of Geodesy. 2019. Vol. 93. Issue 5. P. 635–653. http://dx.doi.org/10.1007/s00190-018-1187-2
12. Wu L., Lin Q. Improved Parker's method for topographic models using Chebyshev series and low rank approximation // Geophysical Journal International. 2017. Vol. 209. Issue 2. P. 1296–1325. https://doi.org/10.1093/gji/ggx093
13. Stolk W., Kaban M., Beekman F., Tesauro M., Mooney W. D., Cloetingh S. 2013, High resolution regional crustal models from irregularly distributed data: Application to Asia and adjacent areas // Tectonophysics. Vol. 602. No. 6. P. 55–68. https://doi.org/10.1016/j.tecto.2013.01.022
14. Buccini A. Tikhonov-type iterative regularization methods for ill-posed inverse problems: theoretical aspects and applications: PhD thesis. Varese, Italy: Università degli Studi dell'Insubria, 2016.
15. Dadak B. Inversion of gravity data for depth-to-basement estimate using the volume and surface integral methods: model and case study. Salt Lake City, UT, USA: The University of Utah, May, 2017. 92 p.
16. Maag E., Li Y. Discrete-valued gravity inversion using the guided fuzzy *c*-means clustering technique // Geophysics. 2018. Vol. 83. Issue 4. P. 1–115. http://dx.doi.org/10.1190/geo2017-0594.1
17. Feng X., Wang W., Yuan B. 3D gravity inversion of basement relief for a rift basin based on combined multinorm and normalized vertical derivative of the total horizontal derivative techniques // Geophysics. 2018. Vol. 83. Issue 5. P. G107–G118. https://doi.org/10.1190/geo2017-0678.1
18. Cella F., Nappi R., Paoletti V., Florio G. Basement Mapping of the Fucino Basin in Central Italy by ITRESC Modeling of Gravity Data // Geosciences. 2021. Vol. 11. No. 10. P. 1–25. https://doi.org/10.3390/geosciences11100398
19. Ren Z., Chen C., Pan K., Kalscheuer T., Maurer H., Tang J. Gravity Anomalies of Arbitrary 3D Polyhedral Bodies with Horizontal and Vertical Mass Contrasts // Surveys In Geophysics. 2017. Vol. 38. No. 2. P. 479–502. https://doi.org/10.1007/s10712-016-9395-x
20. Vatankhah S., Renaut R. A., Huang X., Mickus K., Gharloghi M. Large-scale focusing joint inversion of gravity and magnetic data with Gramian constraint // Geophysical Journal International. 2022. Vol. 230. Issue 3. P. 1585–1611. https://doi.org/10.1093/gji/ggac138
21. Makled W. A., Ashwah A. A. E. E., Lotfy M. M., Hegazey R. M. Anatomy of the organic carbon related to the Miocene syn-rift dysoxia of the Rudeis Formation based on foraminiferal indicators and palynofacies analysis in the Gulf of Suez, Egypt // Marine and Petroleum Geology. 2020. Vol. 111. P. 695–719. https://doi.org/10.1016/j.marpetgeo.2019.08.048
22. Abuzied S. M., Kaiser M. F., Shendi E.-A. H., Abdel-Fattah M. I. Multi-criteria decision support for geothermal resources exploration based on remote sensing, GIS and geophysical techniques along the Gulf of Suez coastal area, Egypt // Geothermics. 2020. Vol. 88. Article number 101893. https://doi.org/10.1016/j.geothermics.2020.101893
23. The Geology of the Arab World – An Overview. Bendaoud A., Hamimi Z., Hamoudi M., Djemai S., Zoheir B. (eds). Berlin: Springer, 2019. 560 p.
24. Temraz M., Dypvik H. The Lower Miocene Nukhul Formation (Gulf of Suez, Egypt): microfacies and reservoir characteristics // Journal of Petroleum Exploration and Production Technology. 2018. Vol. 8. No. 1. P. 85–98. https://doi.org/10.1007/s13202-017-0386-3
25. Van Dijk J., AlBloushi A., Ajayi A. T., De Vincenzi L., Ellen H., Guney H., Holloway P., Khdhaouria M., Mcleod I. S. Hydrocarbon exploration and production potential of the Gulf of Suez Basin in the framework of the new tectonostratigraphic model. SPE Gas & Oil Technology Showcase and Conference (October 21–23, 2019 Dubai, UAE). 2019. Article number SPE-198622-MS. https://doi.org/10.2118/198622-MS

26 Attia I., Helal I., El Dakhakhny A., Aly S. A. Using sequence stratigraphic approaches in a highly tectonic area: Case study – Nubia (A) sandstone in southwestern Gulf of Suez, Egypt // Journal of African Earth Sciences. 2017. Vol. 136. P. 10–21. https://doi.org/10.1016/j.jafrearsci.2017.06.001
27. Farouk S., Sen S., Pigott J. D., Sarhan M. A. Reservoir characterization of the middle Miocene Kareem sandstones, Southern Gulf of Suez Basin, Egypt // Geomechanics and Geophysics for Geo-Energy and Geo-Resources. 2022. Vol. 8. No. 5. P. 1–17. https://doi.org/10.1007/s40948-022-00437-8
28. Embabi A. M., Abdelwahhab M. A., Abdelhafez N. A. Reservoir characterization and petroleum geology at esh el Mallaha field, southern Gulf of Suez, Egypt // Al-Azhar Bulletin of Science. 2021. Vol. 32. No. 2. P. 1–12. https://doi.org/10.21608/absb.2021.89127.1130
29. Hadad Y. T., Hakimi M. H., Abdullah W. H., Kinawy M., El Mahdy O., Lashin A. Organic geochemical characteristics of Zeit source rock from Red Sea Basin and their contribution to organic matter enrichment and hydrocarbon generation potential // Journal of African Earth Sciences. 2021. Vol. 177. Article number 104151. https://doi.org/10.1016/j.jafrearsci.2021.104151
30. The geology of Egypt: Regional Geology Reviews. R. Said (ed.), 2017. 734 p. https://doi.org/10.1201/9780203736678
31. Almalki K. A., Mahmud S. A. Gulfs of Suez and Aqaba: New insights from recent satellite-marine potential field data // Journal of African Earth Sciences. 2018. Vol. 137. P. 116–132. https://doi.org/10.1016/j.jafrearsci.2017.10.004
32. Afifi A. S., Moustafa A. R., Helmy H. M. Fault block rotation and footwall erosion in the southern Suez rift: Implications for hydrocarbon exploration // Marine and Petroleum Geology. 2016. Vol. 76. P. 377–396. https://doi.org/10.1016/j.marpetgeo.2016.05.029
33 Youssef M., El-Sorogy A., El-Sabrouty M., Al-Otaibi H. Invertebrate shells as pollution bio-indicators, Gebel El-Zeit area, Gulf of Suez, Egypt // Indian Journal of Geo-Marine Sciences. 2016. Vol. 45. No. 5. P. 687–695.
35. Ministry of Petroleum and Mineral Resources. Ganoub El-Wadi Petroleum Holding Company “Ganope”. International Bid Round 2016. 2016. P. 1–7.
35. South H. et al. The Source for Critical information and insight. Global Exploration & production service, Gulf of Suez south, Egypt. Status of Carto Data and IRIS21 databases. 2009.
36. Aboud E., Salem A., Ushijima K. Subsurface structural mapping of Gebel El-Zeit area , Gulf of Suez, Egypt using aeromagnetic data // Earth, Planets and Space. 2005. Vol. 57. P. 755–760. http://dx.doi.org/10.1186/BF03351854

Статья поступила в редакцию 08 ноября 2023 года